Lattice Calculation of Hadronic Light-by-Light Contribution to the Muon Anomalous Magnetic Moment

Luchang Jin

Submitted in partial fulfillment of the

requirements for the degree of

Doctor of Philosophy

in the Graduate School of Arts and Sciences

COLUMBIA UNIVERSITY

2016

Abstract

Lattice Calculation of Hadronic Light-by-Light Contribution to the Muon Anomalous Magnetic Moment

Luchang Jin

The quark-connected part of the hadronic light-by-light scattering contribution to the muon's anomalous magnetic moment is computed using lattice QCD with chiral fermions. We report several significant algorithmic improvements and demonstrate their effectiveness through specific calculations which show a reduction in statistical errors by more than an order of magnitude. The most realistic of these calculations is performed with a near-physical, 139 MeV pion mass on a $(5.5\text{ fm})^3$ spatial volume using the $48^3 \times 96$ Iwasaki gauge ensemble of the RBC/UKQCD Collaboration.

Contents

List of Tables

List of Figures

ACKNOWLEDGMENTS

First of all I would like to thank my advisor Prof. Norman Christ for his guidance, insightful discussions and support during my graduate research. The weekly discussion is an reservoir that constantly produces new ideas during the development of this project.

I would also like to thank Prof. Robert Mawhinney for many helpful suggestions and of course help in understanding many physical details. I am grateful to Tom Blum, Peter Boyle, Masashi Hayakawa, Taku Izubuchi, and Chulwoo Jung for guidance, help on testing and advice on numerical analysis and programming.

I enjoyed and benefited from discussions with my colleagues: Ziyuan Bai, Chris Kelly, Christoph Lehner, Zhongjie "Jasper" Lin, Qi Liu, Greg Mclynn, David Murphy, Hantao Yin, Jianglei Yu, Daiqian Zhang, and many others. The results presented here received refinement from many people in the collaboration. I feel myself very fortunate to work in such a great team.

Finally, I would like to thank my family and friends for their uncountable support and understanding throughout these years.

Chapter 1

Introduction

New particles and interactions which occur at a very large energy scale Λ, above the reach of present-day accelerators, may be first discovered through their indirect effects at low energy. To discover these indirect effects, precise measurement and accurate theoretical calculation are needed. One candidate quantity is $g_e - 2$, the electron anomalous magnetic moment. The accuracy of this quantity is usually used as an example to demonstrate the success of quantum field theory. Here g_e, called the gyromagnetic ratio, relates a particle's magnetic moment and its spin:

$$\vec{\mu} = g_e \frac{e}{2m_e} \vec{s} \tag{1.1}$$

This "anomalous" difference between g_e and the Dirac value of 2 for a noninteracting particle comes from quantum corrections. The leading order Feynman diagram is shown in Fig. 1.1. Its value $(g_e - 2)/2 = \alpha/(2\pi) + \mathcal{O}(\alpha^2)$ ($\alpha = e^2/(4\pi)$ is the fine structure constant) was first computed by Julian Schwinger in 1948 and is engraved on his tombstone. g_e can also receive contributions from new high-energy phenomena, contributions which are proportional to the strength of the coupling of these new phenomena to the electron and suppressed by the ratio of the squares of the energy scales $(m_e/\Lambda)^2$. Here $m_e = 0.511$ MeV is the electron mass. We can discover these potential contributions, by comparing the experimental and theoretical

Figure 1.1: Leading order contribtion to $g-2$.

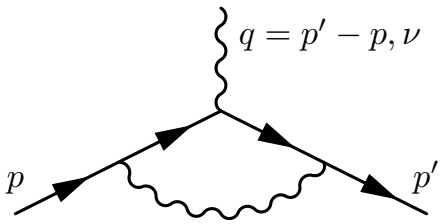

determination of this quantity. The $g_e - 2$ measurement lead by the Harvad group has reached an astonishing precision [11, 12]:

$$a_e \equiv \frac{g_e - 2}{2} = 1159652180.73(0.28) \times 10^{-12} \quad [0.24\text{ppb}], \tag{1.2}$$

here "ppb" means parts per billion. Because of its high accuracy, this value combined with the state of art, complete tenth-order QED calculation [13, 14] is used to determine α. This is the most accurate determination of α to date.

$$\alpha(a_e) = 1/137.0359991570(29)(27)(18)(331) \quad [0.25\text{ppb}]. \tag{1.3}$$

where the uncertainties are from the eighth order QED contribution, tenth order QED contribution, combined hadronic and electroweak contribution, and the measurement of a_e described above, in that order. It can be seen that the theoretical accuracy is even higher than the experiment, and that most of the theoretical error comes from the QED calculation. In order to search for effects from new high-energy phenomena, one may compare this result for $\alpha(a_e)$ with values obtained from other experimental methods. However, even at such a high precision, this result agrees very well with an independently determined α from the Rubidum experiment [15, 16]:

$$\alpha(\text{Rb}) = 1/137.035999049(90) \quad [0.66\text{ppb}]. \tag{1.4}$$

The perfect agreement demonstrates the success and great accuracy of QED. However, this quantity has limited sensitivity to physics at a large energy scale Λ, because of the suppression

factor $(m_e/\Lambda)^2$. A heavier particle, for example, the τ lepton with its mass $m_\tau = 1777$ MeV, would be much more sensitive to high energy effects. However, the lifetime of τ is too short, making accurate measure its magnetic moment very difficult. In fact, the current experiments haven't been able to distinguish $g_\tau - 2$ from zero [17].

A particularly promising low-energy quantity that may reveal such effects is the anomalous moment of the muon. Its mass $m_\mu = 106$ MeV is much heavier than that of the electron while it has a long enough lifetime to allow an accurate measurement of its magnetic moment. The known couplings of the muon are its relatively weak interaction with the photon, the $W^\pm$, Z and Higgs bosons, which can be accurately described by perturbation theory. This implies that even very small differences between $g_\mu - 2$ and the predictions of the standard model can be recognized, making $g_\mu - 2$ an attractive place to search for new, beyond-the-standard-model phenomena [18].

In fact, the use of $g_\mu - 2$ to search for new phenomena has reached a very high level of precision. This quantity has been measured with an accuracy of 0.54 ppm [19] and the corresponding theoretical calculations have achieved a similar level of precision. The present status of experiment and theory is summarized in Table 1.1. As this table shows there is at present a 3 standard deviation discrepancy between the experimental result and the standard model prediction. This discrepancy provides strong motivation both for new experiments, which are either underway or planned at Fermilab (E989) and J-PARC (E34) with a targeted precision as small as 0.14 ppm, and for a reduction in the theoretical errors.

The two components of the theoretical calculation with the largest errors involve couplings to the up, down and strange quarks: the hadronic vacuum polarization (HVP) and hadronic light-by-light scattering (HLbL). These are the first cases in which the effects of the strong interaction enter the determination of $g_\mu - 2$. The HVP effects enter beginning at order α^2 while those from HLbL are of order α^3, where $\alpha = 1/137.036$ is the fine structure constant discussed earlier. These two types of contributions are shown in Fig. 1.2 and, because of the

strong interactions of the quarks, these quantities must be evaluated using methods which treat the strong interactions nonperturbatively.

Table 1.1: Comparison between experiment and the standard model prediction for $(g_\mu - 2)/2$ (in units of 10^{-11}). Other recent analyses [1, 2] give similar values for the difference between experiment and standard model theory. Note that the HVP NNLO contribution is not included in the standard model totals, while LO, NLO and NNLO indicates leading order, next-leading order and next-next-leading order.

SM Contribution	Value ± Error	Ref
QED (incl. 5-loops)	116584718.951 ± 0.080	[20]
HVP LO	6949 ± 43	[2]
HVP NLO	-98.4 ± 0.7	[2, 21]
HVP NNLO	12.4 ± 0.1	[21]
HLbL	105 ± 26	[7]
Weak (incl. 2-loops)	153.6 ± 1.0	[22]
SM Total (0.51 ppm)	116591840 ± 59	[20]
Experiment (0.54 ppm)	116592089 ± 63	[19]
Difference (Exp − SM)	249 ± 87	[20]

The strong-interaction contribution to HVP can be determined directly from the experimentally measured cross section for the single-photon $e^+ - e^-$ annihilation into hadrons using a dispersion relation — a well-developed method with fractional percent errors. These same nonperturbative strong-interaction effects can be determined using lattice QCD [23] but accuracy comparable to that obtained from experimentally measured $e^+ - e^-$ annihilation has yet to be achieved. The determination of the HVP contribution by both methods is an active area of research [24, 25]. Quark-disconnected diagrams, if present, are usually

considerred to be the most difficult part of a lattice calculation, because the statistical error for disconnected diagram is usually much harder to control compared with those for connected diagrams. Recently, the disconnected diagram for HVP contribution has been computed with absolute accuracy similar to the current experimental result [26]. Various noise reduction techniques were used to obtain such high accuracy. These include all-to-all propagators [27], AMA method [28, 29], and diluted random volume sources. In particular, the strong cancelation between the high-mode parts of the light quark contribution and the strange quark contribution was important to obtain the desired accuracy. The next critical part of the HVP calculation is the light quark connected diagram contribtution. With all-to-all propagators and AMA method, accuracy comparable to the experimental result may be achieved in the near future. Computing the connected diagram contribution from other, heavier flavors of quarks is easier. Isospin breaking and electro-magnetic corrections, while involving many more complex diagrams, shouldn't be an real obstucle, because the statistical errors are relatively easy to control.

Figure 1.2: Feynman diagrams depicting the hadronic vacuum polarization (left) and hadronic light-by-light scattering (right) contributions to $g_\mu - 2$.

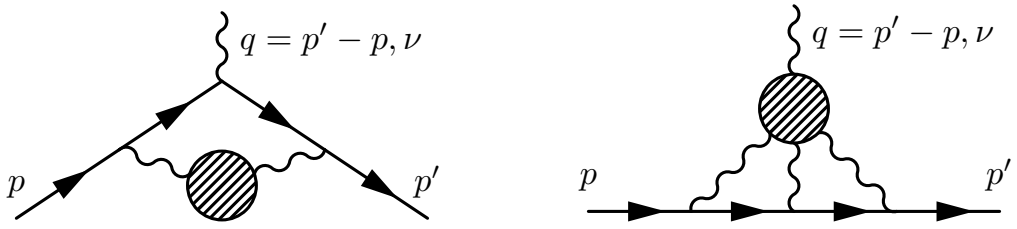

The HLbL contribution is less well studied and is the topic of this thsis. Unlike the HVP case, it is presently not known how to determine the HLbL contribution from experimental data and dispersion relations, although progress is being made in this direction [30, 31, 32, 33, 34]. The HLbL contribution to $g_\mu - 2$ has been evaluated in model calculations [7, 25] whose errors cannot be systematically improved and whose estimates, which are used in Table 1.1, are approximately the same size as the discrepancy between the standard model

theory and experiment.

However, as demonstrated by Blum, Chowdhury, Hayakawa and Izubuchi [8], this quantity can be calculated from first principles using the methods of lattice QCD. Unfortunately, as their calculation also demonstrates, even the most accessible quark-connected part of the HLbL contribution is a challenging task for lattice QCD, especially if physical quark masses and realistically large volumes are to be used. The more difficult disconnected parts, while also accessible to a first-principles lattice calculation, will be even more demanding.

In the present thesis we develop a series of significant improvements to the methods used in the paper of Blum *et al.* and demonstrate their effectiveness with several calculations, including one at physical, 139 MeV pion mass in a large $(5.5\text{ fm})^3$ spatial volume. These improvements are described as a series of steps which reduce both systematic and statistical errors while giving greater insight into the quantity being computed. In this thesis we will mostly focus on the connected HLbL amplitude, which will be abbreviated as cHLbL.

In the first step (Sec. 3.1), we move from the nonperturbative treatment of QED used in Ref. [8] to one in which explicit stochastic electromagnetic fields are introduced which generate only the three photon propagators which appear in the $O(\alpha^3)$ HLbL amplitude. This avoids entirely $O(\alpha^2)$ statistical errors as well as the unwanted $O(\alpha^4)$ contributions present in the earlier, nonperturbative approach to QED.

In the second step (Sec. 3.2), these stochastically generated photon propagators are replaced by the analytic propagators which they approximate. Of course, when making such a replacement, we lose the important benefit offered by the stochastic approach: when a photon propagator is generated as the average of a product of stochastic fields, the complete amplitude can be written as the product of separate factors, one containing the source field and the other the sink field. It is only when this product is averaged over the stochastic field that a coupling between these factors is introduced. A calculation of $(\text{volume})^2$ difficulty is replaced by the average of products, each of only $(\text{volume})^1$ difficulty.

We overcome the (volume)^3 problem that results when three analytic photon propagators are introduced, by stochastically summing over the locations where two of the photons couple to the internal quark line. For example, referring to Fig. 1.3, we might evaluate each amplitude for a series of random space-time locations of the vertices at x and y and then stochastically sum over x and y. This replacement of a stochastic evaluation of the $4L^3T$-dimensional integral over the electromagnetic field by the much simpler stochastic evaluation of the 8-dimensional sum over two electromagnetic vertices dramatically simplifies the calculation. Here L and T are the spatial and temporal extents of the lattice volume. Since the two vertices appear on the same closed quark loop, the amplitude being evaluated will fall exponentially as x and y are separated beyond ≈ 1 fm, a fact that can be exploited when choosing the distribution according to which x and y are generated.

Figure 1.3: Hadronic light-by-light diagrams. There are four additional diagrams resulting from further permutations of the photon vertices on the muon line.

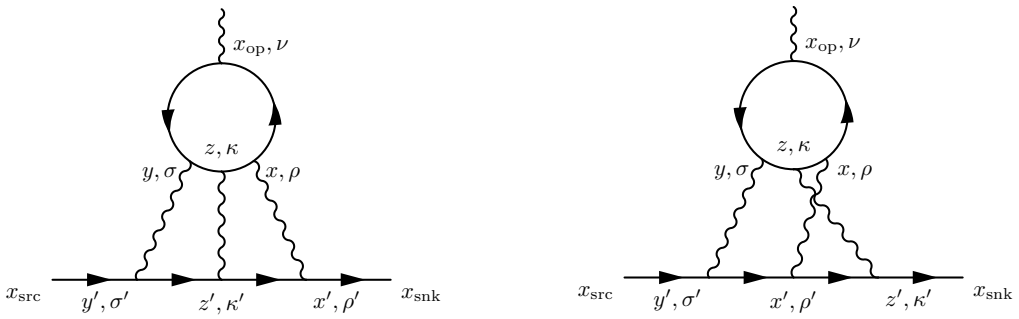

As is shown in Appendix A, the short-distance properties of these HLbL graphs require that at least one of the currents which couple to the internal quark line be a conserved lattice current if the resulting amplitude is to have a simple continuum limit with no need to subtract a contact term. The conservation of the external current implies that this amplitude vanishes in the limit that $q \to 0$, the limit needed to evaluate $g_\mu - 2$. The third algorithmic improvement (Sec. 3.3) that we explore is making a choice of graphs so that this vanishing

behavior in the $q \to 0$ limit occurs for each QCD gauge configuration. If this approach is adopted, then both the signal and the noise will vanish in this limit.

The fourth algorithmic development (Sec. 3.4) resolves the difficulty of evaluating the limit $q^2 \to 0$ for an amplitude which is proportional to q in finite volume. In such a case the amplitude would normally be evaluated at the smallest, nonzero lattice momentum $2\pi/L$ and the limit $q^2 \to 0$ achieved only in the limit of infinite volume (or by extrapolation from nonzero q^2). Here we introduce a position-space origin related to the choice of x and y and show that a simple, spatial first moment of the finite-volume, current matrix element between zero-momentum initial and final muons will yield the $q^2 = 0$ anomalous magnetic moment:

$$(g_\mu - 2)_{\mathrm{cHLbL}} \frac{-e}{4m_\mu} \vec{\sigma}_{s's} = \frac{1}{2} \int d^3r \left\{ \vec{r} \times \left\langle \mu(s') \right| \vec{J}(\vec{r}) \left| \mu(s) \right\rangle_{\mathrm{cHLbL}} \right\}. \tag{1.5}$$

Here $\vec{\sigma}$ is a vector formed from the three Pauli matrices, s and s' are the initial and final spin indices and the label cHLbL indicates that only the quark-connected, HLbL amplitude is being considered. The relation between the initial and final states, the electromagnetic current $\vec{J}(\vec{r})$ and the volume will be carefully specified below.

The thesis is organized as follows: In Chapter 2 we give a short description for lattice QCD. In Chapter 3 we describe in greater detail the algorithmic improvements outlined above. Chapter 4 contains the numerical results that demonstrate these new methods. Two results are of particular interest. The first is a value for the quark-connected HLbL contribution:

$$\frac{(g_\mu - 2)_{\mathrm{cHLbL}}}{2} = (0.0933 \pm 0.0073)(\alpha/\pi)^3 = (116.9 \pm 9.1) \times 10^{-11}, \tag{1.6}$$

obtained with a 139 MeV pion mass and $(5.5\ \mathrm{fm})^3$ volume, the most realistic lattice QCD calculation of this quantity to date. While it is premature to compare this result with experiment or model calculations because the errors arising from finite-volume, finite-lattice spacing, and the quark-disconnected diagram contribution are not yet controlled, the 8% statistical error suggests that this calculation is now within the reach of the methods of

lattice QCD. The second result of special interest is for pure QED where a muon loop instead of a quark loop appears. In this case all of the diagrams are connected so our calculation should give the complete result. Here we work at $q^2 = 0$ and examine three values for the lattice spacing a (actually three values of $m_\mu a$) and three physical volumes. We use the three choices of lattice spacing to extrapolate to the continuum limit and are then able to recognize a $1/L^2$ dependence on the spatial extent L of the volume. Using this form to extrapolate to $L \to \infty$, we obtain a continuum and infinite volume limit which is consistent with the known, perturbative QED result. In Chapter 5, we discuss three major systematic effects in the previous physical pion mass calculation, namely absent of quark disconnected, finite volume effect, and discretization effect. A summary and outlook are given in Chapter 6. We should emphasize that as in Ref. [8], only the quark-connected HLbL contribution has been considered and the quark-disconnected diagrams, where two, three, or four quark loops couple to the external current and the three internal photon propagators, are not discussed.

Chapter 2

Lattice QCD

Lattice is a method to regularize the quantum field theory. Comparing with other regularization scheme, like dimensional regularization, lattice regularization provide a non-perturbative definition for the theory. In fact, it is currently the only known method to define a quantum field theory non-perturbatively. This property is very important for the theory of strong interaction, QCD. Its large coupling constant in low energy region requires non-perturbative treatment. Even at high energy, because of confinement, one also need to deal with the non-perturbative aspect of the interactions of the color neutral bound states. For the electro-weak interaction, the coupling constant is small, perturbation theory is successful and most phenomena can be explained with perturbation calculation. But having a non-perturbative definition would still be satisfactory theoretically. More over, some phenomena, especially ones related with instantons, require a non-perturbative description. However, inventing a lattice formulation for electro-weak interaction, which is a chiral gauge theory, is still an open problem. Several proposals have been made with the hope that the problem can be solved [35, 36, 37, 38, 39].

In this chapter we give a short introduction to the lattice QCD. A more complete, pedagogical discussion on this topic can be found in [40]. In Section 2.1, we introduce the lattice QCD partition function. In Section 2.2, we describe the gauge action we used our gauge

ensemble. We then describe the fermion action in Section 2.3.

2.1 Partition function

The partition function plays a central role in the lattice formulation. Here, we introduce the partition function that is used in generating most of our configurations, which include all the ensembles used in this thesis.

$$\begin{aligned} Z &= \int [\mathcal{D}U_\mu] e^{-S_G[U]} \int [\mathcal{D}\bar{u}][\mathcal{D}u][\mathcal{D}\bar{d}][\mathcal{D}d][\mathcal{D}\bar{s}][\mathcal{D}s] \\ &\quad \cdot \exp(\bar{u}D[m_l, U]u + \bar{d}D[m_l, U]d + \bar{s}D[m_s, U]s) \\ &= \int [\mathcal{D}U_\mu] e^{-S_G[U]} \det(D[m_l, U])^2 \det(D[m_s, U]), \end{aligned} \tag{2.1}$$

where U_μ is SU(3) matrix which represent the gauge field, $S_G[U]$ is the gauge action, $D[m, U]$ is the Dirac operator, and $m_l = (m_u + m_d)/2$. $\bar{u}$, u, $\bar{d}$, d, $\bar{s}$, s are independent sets of anti-commute Grassmann numbers. Each of the quantities $\bar{u}$, u, $\bar{d}$, d, and, $\bar{s}$, s are actually fields define on the sites of our four-dimensional space-time lattice. The expectation value of an observable $\mathcal{O}$ can be expressed as:

$$\begin{aligned} \langle \mathcal{O} \rangle &= \frac{1}{Z} \int [\mathcal{D}U_\mu] e^{-S_G[U]} \int [\mathcal{D}\bar{u}][\mathcal{D}u][\mathcal{D}\bar{d}][\mathcal{D}d][\mathcal{D}\bar{s}][\mathcal{D}s] \\ &\quad \cdot \exp(\bar{u}D[m_l, U]u + \bar{d}D[m_l, U]d + \bar{s}D[m_s, U]s)\mathcal{O}. \end{aligned} \tag{2.2}$$

All discussions above are in the context of Euclidean spacetime. However, above expectation value in Euclidean space is equal to the following conventional Hilbert space matrix elements:

$$\langle \mathcal{O} \rangle = \frac{\mathrm{Tr}\left(\mathcal{T}\mathcal{O} \exp\left[-\int_{-T/2}^{T/2} H(t)dt\right]\right)}{\mathrm{Tr}(e^{-HT})}, \tag{2.3}$$

where H is the usual Hamiltonian operator, T is the time extent of the lattice. $\mathcal{T}$ reorders the following operators according to their time labels. $\mathcal{O}$ is usually a product of multiple operators with different time labels. Also, the Hamiltonian operator in the integral is also

attached time label. In fact, the above formula can be viewed as the definition of the Hamiltonian operator.

We use degenerate light quark mass for two reasons: First, since the up quark and down quark masses are both very small, the isospin symmetry is a good approximate symmetry. Second, with the current ensemble generation algorithm, the hybrid Monte Carlo Algorithm, it is much more efficient to compute with the action $\det(D[m_l, U])^2$ instead of action $\det(D[m_u, U])\det(D[m_d, U])$. Electromagnetic effects, which usually have a similar size, are not present in above partition function. If we need to take electromagnetic or isospin symmetry breaking effects into account, they can be included perturbatively.

2.2 Gauge Action

We have two requirements for the gauge action. One is gauge invariance, the other is that the action is local. It is known that any gauge invariant observable can be expressed as a function of Wilson loops. In order to be local, the simplest action is the sum of 1×1 Wilson loops: the plaquettes. This is the Wilson action:

$$S_G[U] = \beta \sum_P \left[1 - \frac{1}{6}\mathrm{Tr}\left(U_P + U_P^\dagger\right)\right]. \tag{2.4}$$

To obtain better continuum limit behavior, one may include a rectangular, 1×2 plaquette term. Our choice is the Iwasaki action:

$$S_G[U] = \beta(1 - 8c_1) \sum_P \left[1 - \frac{1}{6}\mathrm{Tr}\left(U_P + U_P^\dagger\right)\right] \tag{2.5}$$

$$+ \beta c_1 \sum_R \left[1 - \frac{1}{6}\mathrm{Tr}\left(U_R + U_R^\dagger\right)\right], \tag{2.6}$$

where $c_1 = -0.331$. Another common choice is the DBW2 action, which has the same form but set $c_1 = -1.4069$. We do not use the DBW2 action in this study because this action suppresses dislocations too much, which leads to freezing topology.

2.3 Fermion Action

We start by writing down the coordinate index explicitly.

$$\bar{\psi} D[m,U]\psi \;=\; \sum_{x,y} \bar{\psi}(x) D[m,U](x,y)\psi(y). \tag{2.7}$$

A naive discretization of the continuum Dirac operator would be

$$D[m,U](x,y) \;=\; m\delta_{x,y} + \frac{1}{2}\sum_{\mu}\left[\gamma_\mu U_\mu(x)\delta_{x+\mu,y} - \gamma_\mu U_\mu^\dagger \delta_{x-\mu,y}\right]. \tag{2.8}$$

This action is called the naive fermion action. However, this action describes a theory with 16 favors of fermions with degenerate masses. This is usually referred to as the fermion doubling problem, as the number of fermions is doubled for each dimension. One possible way to solve this problem is to take the 16th root of the determinant. It should be noted that, one can construct an local operator, whose determinant exactly equals the 4th root of the naive Dirac operator. The action with this operator is called the staggered fermion action.

Another way to solve the fermion doubling problem is to increase the mass of the doublers by introducing Laplacean term. This is the Wilson fermion action:

$$D_W[m,U](x,y) = (4+m)\delta_{x,y} + \frac{1}{2}\sum_{\mu}\left[(-1+\gamma_\mu)U_\mu(x)\delta_{x+\mu,y} + (-1-\gamma_\mu)U_\mu^\dagger\delta_{x-\mu,y}\right]. \tag{2.9}$$

The down side of this approach is that the chiral symmetry of the continuum formulation when $m \to 0$ is lost, because the Laplacean term breaks chiral symmetry. Although it is believed that the symmetry will be recovered in the continuum limit, one needs to fine tune the mass term to obtain light fermion. Not having explicit chiral symmetry also makes it difficult to study some processes where chiral symmetry plays an important role.

The construction of an action which describes one fermion flavor while also respecting chiral symmetry is not an easy task. It is achieved by introducing a fifth dimension for a massive Wilson fermion, using a technique which causes a massless fermion to emerge on

the boundaries of the fifth dimension [35, 36]. The left and right hand components of the massless fermion live on different sides of the 5-D volume. They can only mix by explicit mass terms or tunnelling all the way though the fifth dimension. The extent of the fifth dimension is called L_s. A "perfect" fermion can be obtained by taking the $L_s \to \infty$ limit. The Domain Wall Fermion (DWF) operator with $L_s = 4$ is given below as an example. It should be straight forward to generalize it to arbitrary L_s.

$$D_{\mathrm{DWF}}[m,U](x,y) = \begin{pmatrix} \delta_{x,y}+D_W & -P_- & 0 & mP_+ \\ -P_+ & \delta_{x,y}+D_W & -P_- & 0 \\ 0 & -P_+ & \delta_{x,y}+D_W & -P_- \\ mP_- & 0 & -P_+ & \delta_{x,y}+D_W \end{pmatrix}, \tag{2.10}$$

where $D_W = D_W[-M_5, U](x,y)$, $P_\pm = (1 \pm \gamma_5)/2$. M_5 is called the domain wall height, it need to be within range $(0,2)$. We set $M_5 = 1.8$ for all the quarks, but set $M_5 = 1$ for the muon, which does not interact with the QCD gauge field.

Although the low modes which live on the boundaries of the fifth dimension mimic the chiral fermion behavior we desire, the massive modes also have some effect on the low energy physics. These effects are suppressed by the large fermion mass, but will eventually be a problem in the $L_s \to \infty$ limit. To fix this problem, we need to introduce corresponding Pauli-Villars terms to cancel the contribution of these heavy 5-D fermions. The resulting partition function becomes:

$$Z = \int [\mathcal{D}U_\mu] e^{-S_G[U]} \frac{\det(D[m_l,U])^2}{\det(D[1,U])^2} \frac{\det(D[m_s,U])}{\det(D[1,U])}, \tag{2.11}$$

where $D = D_{\mathrm{DWF}}$. The expectation value for an observable is:

$$\begin{aligned} \langle \mathcal{O} \rangle = \frac{1}{Z} \int [\mathcal{D}U_\mu] e^{-S_G[U]} \int [\mathcal{D}\bar{u}][\mathcal{D}u][\mathcal{D}\bar{d}][\mathcal{D}d][\mathcal{D}\bar{s}][\mathcal{D}s] \\ \cdot \frac{\exp(\bar{u}D[m_l,U]u + \bar{d}D[m_l,U]d + \bar{s}D[m_s,U]s)}{\det(D[1,U])^3} \mathcal{O}. \end{aligned} \tag{2.12}$$

In some of our calculations, we use Möbius DWF [41] or zMöbius DWF instead of the plain DWF action described above. These actions approximate the original DWF action but

with a smaller L_s, reducing the computational cost without losing the good chiral properties offered by DWF action.

Chapter 3

Evaluation Strategy

The anomalous magnetic moment of the muon is determined by the electromagnetic form factor $F_2(q^2)$ evaluated at $q^2 = 0$: $F_2(0) = (g_\mu - 2)/2 \equiv a_\mu$, where a_μ is known as the muon anomalous magnetic moment and the usual form factors F_1 and F_2 appear in the decomposition of the matrix element of the electromagnetic current between the incoming and outgoing muon states:

$$\langle \mu(\vec{p}\,')|J_\nu(0)|\mu(\vec{p})\rangle \;=\; -e\overline{u}(\vec{p}\,')\Big(F_1(q^2)\gamma_\nu + i\frac{F_2(q^2)}{4m}[\gamma_\nu,\gamma_\rho]q_\rho\Big)u(\vec{p}), \tag{3.1}$$

where $J_\nu(0)$ is the electromagnetic current, $|\mu(\vec{p})\rangle$ and $|\mu(\vec{p}\,')\rangle$ are the initial and final muon states, $u(\vec{p})$ and $\overline{u}(\vec{p}\,') = u^\dagger(\vec{p}\,')\gamma^0$ are standard, positive-energy solutions of the Dirac equation, and $-e$ is the electric charge of the muon. The states $|\mu(\vec{p})\rangle$ and $|\mu(\vec{p}\,')\rangle$ are normalized as simple plane waves. Thus, in finite volume their inner product will be given by $V\delta_{\vec{p},\vec{p}\,'}$ while in infinite volume $(2\pi)^3\delta(\vec{p}-\vec{p}\,')$ will result.

The matrix element in Eq. (3.1) can be obtained from a Euclidean-space lattice QCD calculation by evaluating a Euclidean-space Green's function containing a muon source and sink with definite incoming and outgoing momentum (here chosen to be $-\vec{q}/2$ and $\vec{q}/2$,

respectively) in the limit of large time separation:

$$\mathcal{M}_\nu(\vec{q}) \;=\; \lim_{\substack{t_{\rm src}\to-\infty \\ t_{\rm snk}\to\infty}} e^{E_{q/2}(t_{\rm snk}-t_{\rm src})} \sum_{\vec{x}_{\rm snk},\vec{x}_{\rm src}} e^{-i\frac{\vec{q}}{2}\cdot(\vec{x}_{\rm snk}+\vec{x}_{\rm src})} e^{i\vec{q}\cdot\vec{x}_{\rm op}} \mathcal{M}_\nu(x_{\rm snk},x_{\rm op},x_{\rm src}), \quad (3.2)$$

where $E_{q/2}=\sqrt{(q/2)^2+m_\mu^2}$ and the amplitude $\mathcal{M}_\nu(x_{\rm src},x_{\rm op},x_{\rm snk})$ is given by the Euclidean-space Green's function

$$-e\mathcal{M}_\nu(x_{\rm src},x_{\rm op},x_{\rm snk}) \;=\; \big\langle \mu(x_{\rm snk}) J_\nu(x_{\rm op}) \overline{\mu}(x_{\rm src}) \big\rangle. \quad (3.3)$$

Here the operator $\overline{\mu}(x_{\rm src})$ creates a muon at the space-time position $x_{\rm src}$, $\mu(x_{\rm snk})$ destroys a muon at the position $x_{\rm snk}$ and $J_\nu(x_{\rm op})$ is the operator for the electromagnetic current. For the general case discussed in this and the following paragraph, the fields $\overline{\mu}(x_{\rm src})$ and $\mu(x_{\rm snk})$ must be renormalized, a refinement which is not needed for the class of graphs which enter the HLbL contribution to $g_\mu-2$. Note that the factor $e^{i\vec{q}\cdot\vec{x}_{\rm op}}$ has been introduced into Eq. (3.2) so that translational symmetry implies that $\mathcal{M}_\nu(\vec{q})$ does not depend on the position $x_{\rm op}$.

Recognizing that the two Euclidean-time limits, $t_{\rm src}\to-\infty$ and $t_{\rm snk}\to\infty$ in Eq. (3.2), will project onto physical muon states, we can relate the form factors in Eq. (3.1) and the amplitude $\mathcal{M}_\nu(\vec{q})$:

$$\left[\Big(\frac{-i\not{q}^+ + m_\mu}{2E_{q/2}}\Big)\Big(F_1(q^2)\gamma_\nu + i\frac{F_2(q^2)}{4m}[\gamma_\nu,\gamma_\rho]q_\rho\Big)\Big(\frac{-i\not{q}^- + m_\mu}{2E_{q/2}}\Big)\right]_{\alpha\beta} = \Big(\mathcal{M}_\nu(\vec{q})\Big)_{\alpha\beta}, \quad (3.4)$$

where for clarity we have explicitly introduced the spinor indices α and β and the four-momenta have the form $q^\pm=(iE_{q/2},\pm\vec{q}/2)$.

We now specialize to the cHLbL case of interest and its particular set of six graphs, two of which appear in Fig. 1.3. In this case, it will be convenient to express $\mathcal{M}_\nu(x_{\rm src},x_{\rm op},x_{\rm snk})$ as an explicit sum of an amplitude $\mathcal{F}_\nu(x,y,z,x_{\rm op},x_{\rm snk},x_{\rm src})$ in which the locations of the other three photon-quark vertices, x, y and z, indicated in Fig. 1.3, appear:

$$\mathcal{M}_\nu(x_{\rm src},x_{\rm op},x_{\rm snk}) = \sum_{x,y,z} \mathcal{F}_\nu(x,y,z,x_{\rm op},x_{\rm snk},x_{\rm src}). \quad (3.5)$$

The amplitude $\mathcal{F}_\nu(x, y, z, x_{\rm op}, x_{\rm snk}, x_{\rm src})$ can then be written in terms of quark, muon and photon propagators:

$$\begin{aligned}\mathcal{F}_\nu(x, y, z, x_{\rm op}, x_{\rm snk}, x_{\rm src}) \;&=\\ &-(-ie)^2 \sum_{q=u,d,s} (ie_q)^4 \Big\langle \mathrm{tr}\big[\gamma_\nu S_q\left(x_{\rm op}, x\right) \gamma_\rho S_q(x, z)\gamma_\kappa S_q(z, y)\gamma_\sigma S_q\left(y, x_{\rm op}\right)\big]\Big\rangle_{\rm QCD}\\ &\cdot \mathcal{G}_{\rho\sigma\kappa}(x, y, z, x_{\rm snk}, x_{\rm src}),\end{aligned} \tag{3.6}$$

$$\begin{aligned}\mathcal{G}_{\rho\sigma\kappa}(x, y, z, x_{\rm snk}, x_{\rm src}) \;&=\\ &\sum_{x',y',z'} G_{\rho\rho'}(x, x')G_{\sigma\sigma'}(y, y')G_{\kappa\kappa'}(z, z')\\ &\quad\cdot\Big[S_\mu\left(x_{\rm snk}, x'\right) \gamma_{\rho'} S_\mu(x', z')\gamma_{\kappa'} S_\mu(z', y')\gamma_{\sigma'} S_\mu\left(y', x_{\rm src}\right)\\ &\qquad + S_\mu\left(x_{\rm snk}, z'\right) \gamma_{\kappa'} S_\mu(z', x')\gamma_{\rho'} S_\mu(x', y')\gamma_{\sigma'} S_\mu\left(y', x_{\rm src}\right)\\ &\qquad + \text{four other permutations}\Big],\end{aligned} \tag{3.7}$$

where only the two sets of contractions shown in Fig. 1.3 are written explicitly. For simplicity, Eq. (3.6)(3.7) is written using local operators for each of the seven electromagnetic currents. The electric charge of the muon is $-e$, while $e_u = 2e/3$, $e_d = e_s = -e/3$ are the charges of the up, down and strange quarks. The brackets $\langle \ldots \rangle_{\rm QCD}$ indicate an average over the QCD gauge configurations which provide the background fields in which the quark propagators $S_q(x, y)$ are computed. The quantities $G_{\sigma,\sigma'}(x, y)$ and $S_\mu(x, y)$ are photon and muon propagators, respectively. The polarization indices are shown explicitly on the photon propagators, but S_μ and S_q are 4×4 spinor matrices with the spin indices suppressed. We use Euclidean-space conventions with the γ matrices obeying $\{\gamma_\nu, \gamma_\rho\} = 2\delta_{\nu,\rho}$ as specified in Appendix C.

The six sums over the space-time volume which appear in Eqs. (3.5), (3.6), and (3.7) make this expression too computationally expensive to be evaluated directly, and stochastic methods must be introduced if this quantity is to be computed with current computing resources.

3.1 Stochastic electromagnetic field

One standard stochastic method of including electromagnetic effects is to compute the charged fermion propagators in the background of stochastically generated QED gauge field configurations. If these gauge configurations are generated according to a discrete version of the Maxwell action, then averaging over these QED configurations will reproduce all photon exchange diagrams in exact analogy with the usual technique for including the gluon degrees of freedom in lattice QCD. However, this method will include QED contributions to all orders in α, beginning at order α^1. Since we are only interested in $\mathcal{O}(\alpha^3)$ contributions corresponding to the diagrams in Fig. 1.3, we must perform a carefully crafted subtraction to remove the lower-order contributions while keeping α small to control the higher-order contribution [42]. This method has been successfully applied to obtain the first lattice QCD results for this cHLbL contribution and requires the evaluation of relatively few quantities because of the indirect treatment of most of the electromagnetic degrees of freedom. However, as α is decreased to reduce the size of the unwanted α^4 and higher-order diagrams, we must deal with the lower-order α^2 terms which, although vanishing on average because of the subtractions which are performed, can still contribute to the stochastic noise.

In fact, stochastic methods can be used to directly evaluate the specific graphs of interest if one begins with an expression very similar to the α^3 amplitude of interest given in Eq. (3.6) and (3.7). We can simply replace the photon propagators $G_{\rho,\rho'}(x,y)$ which appear in that equation with the product of two stochastic variables distributed so that the average of their product reproduces the target propagator:

$$\left\langle A_\rho(x) A_{\rho'}(y) \right\rangle_A = G_{\rho,\rho'}(x,y), \tag{3.8}$$

where $\left\langle \ldots \right\rangle_A$ represents an average over this ensemble of electromagnetic gauge fields. An appealing implementation of this approach follows the original construction of Blum *et al.* and replaces only the photon propagators which couple to the left (x) and right (y) points

along the quark line in Fig. 1.3 with stochastic fields while keeping an exact photon propagator which joins the quark line at the center point z. The unwanted propagator joining the points x and y can be avoided if independent stochastic fields are used for the points x and y. If these two stochastic fields are written as $A_\rho(x)$ and $B_\sigma(y)$, then the two diagrams shown in Fig. 1.3 are simplified to those shown in Fig. 3.1.

Figure 3.1: Two of the six HLbL diagrams that result if a stochastic method is adopted to evaluate two of the three photon propagators which appear in Fig 1.3. The wavy line joining the muon line and the quark loop represents the exact photon propagator, while the pairs of factors, $A_\rho^{m_1}(x)$, $A_{\rho'}^{m_1}(x')$ and $B_\sigma^{m_2}(y)$, $B_{\sigma'}^{m_2}(y')$, are the m_1 and m_2 elements of two independent ensembles of stochastic electromagnetic fields.

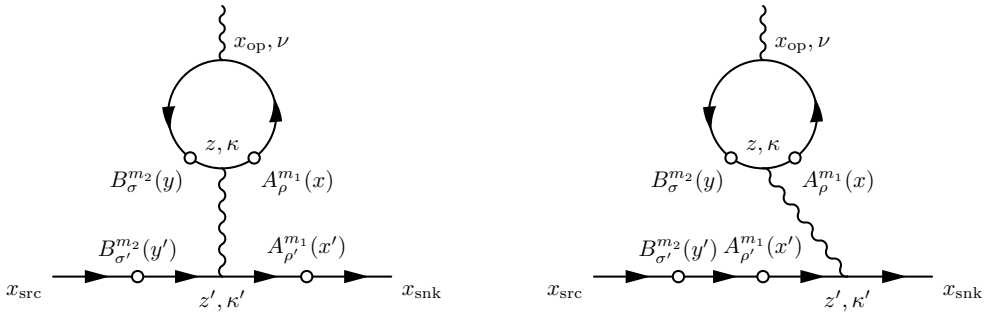

With the introduction of these two stochastic field variables, the evaluation of the amplitudes corresponding to the diagrams shown in Fig. 3.1 is straightforward. Each product of two quark propagators joined by a stochastic field can be evaluated using the sequential-source method. For example, consider the quark propagator on the left side of the loop, coupling to the B^{m_2} field in Fig. 3.1. The location of the external current $x_{\rm op}$ can be used as a source allowing us to solve for the first propagator, $S_q(y, x_{\rm op})$, which is found as a function of the sink position y. This function can then be multiplied by $B_\sigma^{m_2}(y)\gamma_\sigma$ and the resulting function of y used as a source for the second propagator which connects to the vertex z. This same approach can be used to obtain the product of quark propagators joining $x_{\rm op}$ and z,

as well as the two products of pairs of muon propagators needed to construct the muon line. Finally, the resulting two explicit functions of z and z' can be multiplied by the exact photon propagator connecting z and z' and the final sum over z and z' performed with $O(V \ln(V))$ operations by using the fast Fourier transform (FFT).

We should point out that while the discussion above is simplest if we use a fixed location, $x_{\rm op}$ for the external current vertex, in a practical calculation a sum over this position can be achieved by using a random source for the two propagators joined to $x_{\rm op}$, which is distributed over a possibly large space-time subvolume and will lead to a much improved signal-to-noise ratio. In this standard method, arranging the noise source as a vector of independent random numbers for each site guarantees that after a noise average, only the desired terms where the two propagators are joined to the same point will be nonzero.

An interesting enhancement that can be exploited when using this method is to compute the $2M$ sequential-source propagators for the right- and left-hand quark propagators shown in Fig. 3.1 separately, where the right-hand sequential-source propagator incorporates stochastic field A^{m_1}, while the left-hand propagator contains B^{m_2} for $1 \leq m_1, m_2 \leq M$. We can then compute the amplitude of interest for all M^2 pairs, effectively enhancing the statistical sample by a factor of M with only the added cost of M^2 evaluations of the less expensive muonic part of the amplitude. We refer to this approach as the M^2 method and present numerical results in Sec. **??**. These results suggest that the full statistical gain of a factor M^2 is realized.

Introducing specific, stochastic QED fields and using sequential-source propagators solves the problem of lower-order noise that will degrade a dynamical QED calculation in which amplitudes of lower-order in α are removed by subtraction. However, there is another very significant problem, which might be called the "disconnected diagram" problem. If we were to replace all three photon propagators with pairs of stochastic QED fields obeying the condition given in Eq. (3.8), the resulting diagram would usually be referred to as a disconnected

diagram because the quark loop and the muon line are not joined by explicit propagators which decrease as their end points are separated. For example, if we work with fixed spatial locations for $x_{\rm src}$, $x_{\rm op}$ and $x_{\rm snk}$ but allow the time separation $t_{\rm sep}$ between $x_{\rm src}$ and $x_{\rm snk}$ to grow (to project onto the muon ground state), each stochastic field will contribute unsuppressed noise from any point along the muon line. For the case when three stochastic photon propagators are used, these stochastic fluctuations will cause the statistical error to grow as $t_{\rm sep}^{3/2}$, where we estimate the stochastic noise by averaging the square of the product of the three fields evaluated on the muon line, giving a result for the square of the noise which grows proportionally to $t_{\rm sep}^3$. This noise problem will become even more severe if we work in a large spatial volume and use a wall source for the initial and final muon and a random wall source, also at fixed time, for the external current in an attempt to exploit a finite volume average. The result will be a statistical error which should grow as L^3, assuming that L and T are of approximately the same size. (This estimate comes from combining the factor of T^3 obtained in the estimate above with a factor of L^3 resulting from the integration of $x_{\rm op}$ over the L^3 volume contributing at a fixed time, implying an error whose square will grow as T^3L^3.) If one exact photon propagator is introduced as discussed above, these effects are reduced, but the resulting statistical error will still grow as L^2, since the removal of one of the stochastic fields evaluated on the muon line will reduce the T dependence of the square of the error from T^3 to T^2, and the presence of the explicit photon propagator joining the quark loop and muon line will reduce the contribution from the integration over $x_{\rm op}$ from L^3 to L^2.

3.2 Exact photon propagators

To completely avoid this disconnected-diagram problem, we need to use an explicit, free-field formula for each of the three photon propagators and introduce the necessary stochastic sampling in a different way. Fortunately, this is not difficult and will result in statistical noise

that will remain finite, even in the infinite-volume limit. This new approach to the HLbL calculation is the topic of this section. As suggested above, it is not possible to evaluate Eqs. (3.5),(3.6), and (3.7) without approximations even on a single QCD configuration, so we introduce randomness in a different way which, as we will see, leads to statistical fluctuations which are much more easily controlled.

This approach can be best presented if we express the cHLbL amplitude $\mathcal{M}_\nu(\vec{q})$ as an explicit sum over the three additional space-time vertices x, y and z at which the internal photon lines couple to the quark line, in analogy with Eqs. (3.5) and (3.6):

$$\mathcal{M}_\nu(\vec{q}) \;=\; e^{i\vec{q}\cdot\vec{x}_{\rm op}} \sum_{x,y,z} \mathcal{F}_\nu(\vec{q},x,y,z,x_{\rm op}), \tag{3.9}$$

where the factor of $e^{i\vec{q}\cdot\vec{x}_{\rm op}}$ has been introduced so that $\mathcal{M}_\nu(\vec{q})$ will not depend on $x_{\rm op}$, and the amplitude $\mathcal{F}_\nu(\vec{q},x,y,z,x_{\rm op})$ is related to the similar point-source/point-sink quantity defined in Eq. (3.6) by:

$$\mathcal{F}_\nu(\vec{q},x,y,z,x_{\rm op}) \;=\; \lim_{\substack{t_{\rm src}\to-\infty \\ t_{\rm snk}\to\infty}} e^{E_{q/2}(t_{\rm snk}-t_{\rm src})} \sum_{\vec{x}_{\rm snk},\vec{x}_{\rm src}} e^{-i\frac{\vec{q}}{2}\cdot(\vec{x}_{\rm snk}+\vec{x}_{\rm src})} \mathcal{F}_\nu(x,y,z,x_{\rm op},x_{\rm snk},x_{\rm src}). \tag{3.10}$$

Here we will choose the momentum transfer $\vec{q} = (2\pi/L)\hat{z}$, where $\hat{z}$ is a unit vector in the z direction. Thus, the muon propagators must be evaluated with antiperiodic boundary conditions in the z direction. As observed previously, translational symmetry in the three spatial directions and the added factor of $e^{i\vec{q}\cdot\vec{x}_{\rm op}}$ introduced in Eqs. (3.2) and (3.10) imply that the right-hand side of Eq. (3.9) is independent of $\vec{x}_{\rm op}$. Similarly, the right-hand side of Eq. (3.9) does not depend on $t_{\rm op}$, since the energies of the initial and final muons are the same.

We can exploit the space-time translational covariance of $\mathcal{F}_\nu(\vec{q},x,y,z,x_{\rm op})$ to write the sum in Eq. (3.9) in terms of variables expressed relative to the location of the quark loop.

Begin by shifting all four position arguments of this function by the average $w = (x+y)/2$:

$$\mathcal{M}_\nu(\vec{q}) = \sum_{x,y,z} e^{i\vec{q}\cdot(\vec{x}_{\rm op}-\vec{w})}\mathcal{F}_\nu\left(\vec{q}, \frac{x-y}{2}, -\frac{x-y}{2}, z-w, x_{\rm op}-w\right) \tag{3.11}$$

$$= \sum_r \left\{ \sum_{\widetilde{z},\widetilde{x}_{\rm op}} e^{i\vec{q}\cdot\vec{\widetilde{x}}_{\rm op}}\mathcal{F}_\nu\left(\vec{q}, \frac{r}{2}, -\frac{r}{2}, \widetilde{z}, \widetilde{x}_{\rm op}\right)\right\}, \tag{3.12}$$

where in the second equation we have changed summation variables to

$$r = x - y, \quad \widetilde{z} = z - w \quad \text{and} \quad \widetilde{x}_{\rm op} = x_{\rm op} - w \tag{3.13}$$

and explicitly organized the sums so that the sum over the relative coordinate r is performed last.

The form of Eq. (3.12) suggests a natural strategy for its evaluation in lattice QCD. First we make a random choice of the average variable w somewhere within the space-time volume of our simulation. To match our assumption that $t_{\rm snk} - t_{\rm op}$ and $t_{\rm op} - t_{\rm src}$ are large we choose the times $t_{\rm snk}$ and $t_{\rm src}$ to be $(x_{\rm op})_0 + T/4$ and $(x_{\rm op})_0 - T/4$, respectively, where the sums should be performed modulo T, the temporal extent of the lattice volume. Next, the space-time variable r is chosen stochastically as described below, and the points $r/2$ and $-r/2$ are used as source locations for two propagators whose sinks are joined at the positions $\widetilde{z}$ and $\widetilde{x}_{\rm op}$, which are then explicitly summed over the entire lattice. The resulting $\mathcal{M}_\nu(\vec{q})$, when summed over w and r and averaged over gauge configuration, is the desired muon-current three-point function.

To evaluate the stochastic sum over r efficiently, we use importance sampling, *i.e.* we sample most frequently the important region where $|r| \lesssim 1$ fm. For some of the results presented here we choose a set of M points $\{x_i\}_{1\le i\le M}$ following the empirically chosen distribution:

$$p\big(|x_i - w|\big) \propto \begin{cases} 1 & |x_i - w| < 1 \\ 1/|x_i - w|^{3.5} & |x_i - w| \geqslant 1 \end{cases}, \tag{3.14}$$

where the special treatment when $|x_i - w|$ is smaller than one lattice unit has been introduced to avoid the singularity in our distribution at $x_i - w = 0$. The distribution of the relative distance $|r|$ between any two points drawn from this set is

$$P(|r|) \;=\; \sum_x p\big(|x-r|\big)p\big(|x|\big). \tag{3.15}$$

The resulting distribution $P(|r|)$ used for our $32^3 \times 64$ ensemble is shown in Fig. 3.2.

Figure 3.2: Distribution of relative separations $|r| = |x-y|$ between the x-y pairs of randomly chosen points used to compute $\mathcal{M}_\nu(\vec{q})$ on the $32^3 \times 64$ QCD gauge ensemble described in Sec. 4.3

.

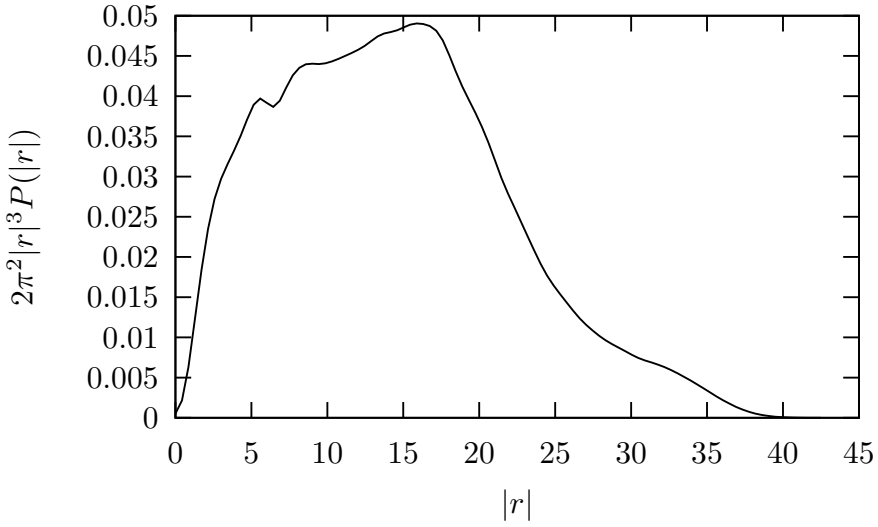

Note that $M(M-1)/2$ x-y pairs can be formed from a set of M points. (Here each "pair" is already symmetrized between the points x and y.) If we calculate a single, point-source quark propagator for each of these M points, then for each x-y pair, we can sum over $\widetilde{z}$ and $\widetilde{x}_{\rm op}$ exactly with no further inversions. We find that the resulting statistical error corresponds to that from the larger number of M^2 samples unless M is so large that these many samples, all distributed within $\approx 1/m_\pi$ of the single point w become correlated. This M^2 benefit is seen for M at least as large as 16.

In contrast with the stochastic electromagnetic field discussed in Sec. 3.1, the statistical noise in the exact-photon-propagator method remains finite in the infinite-volume limit because the quark propagator decreases exponentially with distance. The noise associated with the stochastic sampling of the space-time points x and y will also fall as $1/\sqrt{N}$ in the limit of a large number N of x-y samples provided the distribution $P(|r|)$ that we choose is normalizable in the infinite-volume limit, a choice which is certainly possible, again because the quark propagator decreases exponentially with distance.

This exact photon propagator method gives a very large reduction in statistical errors when compared to the previous methods based on a stochastic photon field and is the basis for the $m_\pi = 139$ MeV, $(5.5 \text{ fm})^3$ volume calculation reported in the next section. The replacement of a stochastic average over $4L^3T$ gauge variables by the simpler importance sampling of two 4-dimensional space-time positions r and w results in a calculation that appears easier to optimize. We learn *a posteriori* how the integrand depends on $|r|$ and can adjust our sampling weights to increase the effectiveness of the sampling. In particular, we recognize that the largest integrand results from small $|r|$ and therefore compute all pairs with $|r| \leqslant r_{\max}$. A similar advantage from the use of exact photon propagators may be found when this approach is applied to other processes which include electromagnetism.

3.3 Current conservation on each configuration

As can be seen from Eq. (3.1), the form factor $F_2(q^2)$ from which $g_\mu - 2$ can be determined is proportional to q, which implies that the signal that results from our Monte Carlo average will vanish in the $q \to 0$ limit that is needed to determine $F_2(0)$. However, the form shown in Eq. (3.1), and especially the proportionality to q, is a consequence of the conservation of the current J_ν, a condition that will not be obeyed for the individual samples that are averaged in the exact-photon-propagator method described in the previous section.

As discussed in Appendix A, if at least one of the four currents coupled to the quark loop

is exactly conserved at finite lattice spacing, the HLbL amplitude will be convergent and have a correct continuum limit. We meet this requirement by using the exactly conserved, five-dimensional DWF current as the external current $J_\nu(x_{\rm op})$. This guarantees that the resulting amplitude will have the form given in Eq. (3.1) up to finite lattice spacing corrections. However, for the method described in the previous section, the vertices x, $x_{\rm op}$, y and z appear in a specific order on the quark loop. We have not computed all three possible insertions for the external photon. Consequently, the individual samples will not yield a conserved current. The Ward identity necessary for the external current to have a vanishing divergence will be obeyed only after the stochastic average over x and y, which makes the three internal photon vertices on the quark line indistinguishable. As a result, the noise will not vanish when $q = 0$.

Figure 3.3: Diagrams showing the three different possible insertions of the external photon when the vertices x and y are fixed. For each of these three diagrams, there are five other possible permutations of the connections between the three internal photons and the muon line that are not shown. The contributions of each of these three sets of six contractions will be the same after the stochastic average over the vertices x and y.

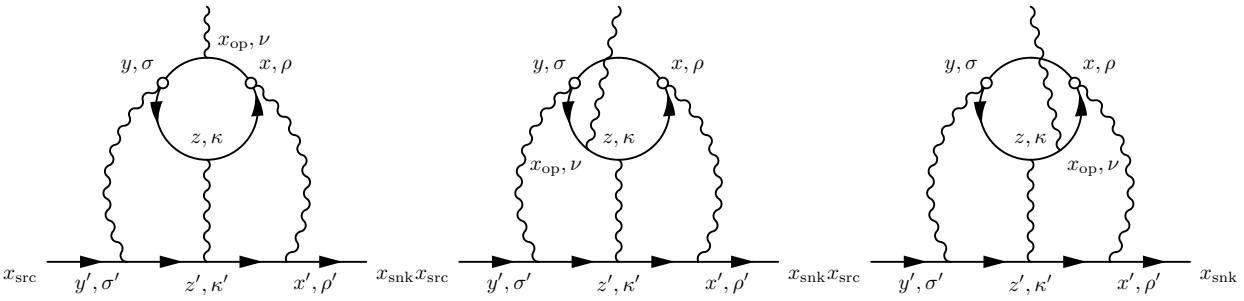

To make the contribution of each configuration (and hence the statistical noise) vanish as $q \to 0$, we must average the three diagrams in Fig. 3.3 so that the required Ward identity

is obeyed, configuration by configuration [1]. Explicitly, this average can be achieved by replacing the function $\mathcal{F}_\nu$ of Eq. (3.6) with the symmetrized version $\mathcal{F}_\nu^C$ given by

$$\begin{aligned}\mathcal{F}_\nu^C&\left(x,y,z,x_{\rm op},x_{\rm snk},x_{\rm src}\right)\\&=\frac{1}{3}\mathcal{F}_\nu\left(x,y,z,x_{\rm op},x_{\rm snk},x_{\rm src}\right)+\frac{1}{3}\mathcal{F}_\nu\left(y,z,x,x_{\rm op},x_{\rm snk},x_{\rm src}\right)\\&\quad+\frac{1}{3}\mathcal{F}_\nu\left(z,x,y,x_{\rm op},x_{\rm snk},x_{\rm src}\right).\end{aligned}\tag{3.16}$$

In later equations, we will simply add the superscript C to indicate that such an average has been performed. These additional diagrams are also computationally accessible. The left-hand diagram represents the single amplitude that would be computed following the method of Sec. 3.1. The center diagram requires the computation of sequential-source propagators at $x_{\rm op}$ for each polarization of the external photon. Finally the right-hand diagram also requires sequential-source propagators at $x_{\rm op}$, but with the external photon momentum in the opposite direction, since γ_5 Hermiticity must be used to reverse the direction of the propagators, which reverses the momentum of the external photon as well.

Thus, in addition to the point-source propagators from the sites x and y, we must compute sequential-source propagators as discussed in Sec. 3.1 for each possible polarization and momentum of the external current. We normally evaluate the amplitude for three polarization directions x, y, and t (which are perpendicular to the z direction of the external momentum) and two momentum directions (since in some cases the complex conjugate of the sequential-source propagator is needed). This requires an additional 6 times more quark Dirac-operator inversions. Since we can adjust M to rebalance the cost, the overall cost increase may not be significant, but the potential gain can be large, especially in a large volume when we study small $q = 2\pi/L$.

[1] Although current conservation is exact, in a finite lattice volume with periodic boundary conditions, around the world effects will contribute to the signal and the noise even when the external momentum is zero. However, this noise is suppressed exponentially in the large volume limit. In summary, in the small q and large volume limit, the noise will behave as $\mathcal{O}(q) + \mathcal{O}(e^{-m_\pi L/2})$.

There is an additional optimization that can be exploited when all three groups of the diagrams represented in Fig. 3.3 are computed. Since the three internal photon vertices are now treated symmetrically, we are free to introduce one asymmetry and restrict the sum over the z vertex to the region where $|x-y| < |x-z|$ and $|x-y| < |y-z|$ and multiply the result by 3 [2]. This restriction on z will skew the distribution of $|x-y|$ enhancing the region where $|x-y|$ is small and the signal less noisy, but suppressing the large $|x-y|$ region where the signal is weak and the noise large.

3.4 Moment method: Obtaining $q^2 = 0$ in finite volume

As can be seen in Eq. (3.1), a matrix element of the current $J_\nu(x_{\rm op})$ between muon states contains the electromagnetic form factor $F_2(q^2)$ multiplied by components of the momentum transfer q_ρ. This suggests that $F_2(q^2)$ can be obtained in a lattice calculation only when $q_\beta \neq 0$, so the anomalous moment $g_\mu - 2 = 2F_2(0)$ can be determined only after taking the limit $q_\rho \to 0$. Of course, this limit is difficult to evaluate in a lattice calculation since the smallest nonzero momentum component is $2\pi/L$, suggesting that $F_2(0)$ will only become accessible if very large spatial lattice sizes are studied. We will now show how this potential difficulty can be avoided for the case of the light-by-light contribution to $g_\mu - 2$ by evaluating a carefully defined spatial moment of the Feynman amplitude which determines the matrix element of $J_\nu(x)$.

We begin with Eq. (3.12) repeated here with a small change in notation:

$$\mathcal{M}_\nu(\vec{q}) \;=\; \sum_{r,z,x_{\rm op}} \mathcal{F}^C_\nu\Big(\vec{q}, \frac{r}{2}, -\frac{r}{2}, z, x_{\rm op}\Big) e^{i\vec{q}\cdot\vec{x}_{\rm op}}, \tag{3.17}$$

where we have altered that earlier equation by dropping the tilde on the summation variables z and $x_{\rm op}$ and adding the superscript C. Note that the function $\mathcal{F}^C$ has the same dependence

[2] The necessary combinatoric factor is also introduced for the boundary cases where $|x-y| = |x-z|$ or $|x-y| = |y-z|$.

on $x_{\rm op}$ as does the current $J_\nu(x_{\rm op})$ whose matrix element is being evaluated and will therefore obey the same Ward identity:

$$\Delta_{(x_{\rm op})_\nu}\mathcal{F}_\nu^C(\vec{q},x,y,z,x_{\rm op})=0, \tag{3.18}$$

where a sum over the repeated index ν is understood and Δ_x evaluates the "backward" lattice difference:

$$\Delta_x f(x)=f(x)-f(x-a), \tag{3.19}$$

where a is the lattice spacing.

The critical step in our presentation replaces the factor $e^{i\vec{q}\cdot\vec{x}_{\rm op}}$ in Eq. (3.17) with $(e^{i\vec{q}\cdot\vec{x}_{\rm op}}-1)$, giving

$$\mathcal{M}_\nu(\vec{q})=\sum_{r,z,x_{\rm op}}\mathcal{F}_\nu^C\Big(\vec{q},\frac{r}{2},-\frac{r}{2},z,x_{\rm op}\Big)\big(e^{i\vec{q}\cdot\vec{x}_{\rm op}}-1\big). \tag{3.20}$$

The extra "-1" term introduced into the sum over $x_{\rm op}$ will vanish because of the Ward identity, Eq. (3.18), if a surface term can be neglected. This can be seen from the following manipulation:

$$\begin{aligned}
0 &= \sum_{x_{\rm op}}\Delta_{(x_{\rm op})_\rho}\left((x_{\rm op})_\nu\mathcal{F}_\rho^C\left(\vec{q},\frac{r}{2},-\frac{r}{2},z,x_{\rm op}\right)\right) &(3.21)\\
&= \sum_{x_{\rm op}}\left\{\mathcal{F}_\nu^C\left(\vec{q},\frac{r}{2},-\frac{r}{2},z,x_{\rm op}\right)+(x_{\rm op})_\nu\Delta_{(x_{\rm op})_\rho}\mathcal{F}_\rho^C\left(\vec{q},\frac{r}{2},-\frac{r}{2},z,x_{\rm op}\right)\right\} &(3.22)\\
&= \sum_{x_{\rm op}}\mathcal{F}_\nu^C\left(\vec{q},\frac{r}{2},-\frac{r}{2},z,x_{\rm op}\right), &(3.23)
\end{aligned}$$

where the final line demonstrates that the extra "-1" term that was added to Eq. (3.17) sums to zero.

Finally we can expand the right-hand side of Eq. (3.20) in q_ρ and determine

$$\frac{\partial}{\partial q_i}\mathcal{M}_\nu(\vec{q})|_{\vec{q}=0}=i\sum_{r,z,x_{\rm op}}\mathcal{F}_\nu^C\Big(\vec{q}=0,r,-r,z,x_{\rm op}\Big)(x_{\rm op})_i. \tag{3.24}$$

While this equation has been derived in infinite space-time volume, the fact that the average of the two points r and $-r$ is located at the origin implies that the integrand decreases

exponentially as $|x_{\rm op}|$ increases, so this integral can be evaluated in finite volume with only exponentially small corrections.

As discussed in Sec. 3.3, Eq. (3.18) representing current conservation is somewhat subtle. This equation with the fixed vertices $\pm r$ and z will only be obeyed if the external current $J_\nu(x_{\rm op})$ is inserted in all possible places along the internal quark loop. This requires that all three diagrams shown in Fig. 3.3 be included. This requirement that all three diagrams must be included remains valid even if we perform the integration over the four-vectors r and z. Since the midpoint of the vertices $\pm r$ remains at the origin, these two $\pm r$ vertices remain distinguished, and the cancellation required to derive the Ward identity for a closed fermion loop will not be realized unless all three diagrams are combined.

A further refinement of this approach which we have not yet explored numerically, chooses the origin with respect to which $x_{\rm op}$ is defined not as the average of the two points x and y but instead as the average of the three points x, y and z. With this more symmetrical choice of the origin, the necessary Ward identity would hold when the six possible contractions to the muon line are included and the points x and y stochastically summed. This approach would then allow us to avoid the calculation of the additional six sequential-source propagators that are required when all three diagrams of Fig. 3.3 must be computed.

We can obtain a complete expression for $F_2(0)$ and hence $g_\mu - 2$ from Eq. (3.17) by performing a similar small-q expansion of Eq. (3.4). For the light-by-light diagram in the small momentum transfer limit, we can specialize Eq. (3.4)

$$\left(\frac{-i\not{q}^+ + m_\mu}{2E_{q/2}}\right)\left(\frac{F_2(q^2)}{2m_\mu}\frac{i}{2}[\gamma_\nu,\gamma_\beta]q_\beta\right)\left(\frac{-i\not{q}^- + m_\mu}{2E_{q/2}}\right) = \mathcal{M}_\nu(\vec{q}), \tag{3.25}$$

where the external four-momenta $q^\pm = (iE_{q/2}, \pm\vec{q}/2)$. If we examine the case $\nu = i$, equate the coefficients of $(\vec{q})_j$, and evaluate the matrix element of this equation between Dirac positive-energy, zero-momentum eigenstates, we find

$$\overline{u}(\vec{q}=\vec{0},s')\left(\frac{F_2(q^2=0)}{2m_\mu}\frac{i}{2}[\gamma_i,\gamma_j]\right)u(\vec{q}=\vec{0},s) = \overline{u}(\vec{q}=\vec{0},s')\frac{\partial}{\partial q_j}\mathcal{M}_i(\vec{q})_{\vec{q}=\vec{0}}u(\vec{q}=\vec{0},s). \tag{3.26}$$

Finally we can multiply the left- and right-hand sides of this equation by $\frac{1}{2}\epsilon_{ijk}$, sum over i and j and use Eq. (3.24) to replace the derivative of $\mathcal{M}(\vec{q})$ with respect to q_j with the moment of $\mathcal{F}^C$ times $(x_{\rm op})_j$. The result is the kth component of the vector equation:

$$\frac{F_2(0)}{2m_\mu}\overline{u}(\vec{0},s')\,\vec{\Sigma}\,u(\vec{0},s) = \frac{1}{2}\sum_{r,z,x_{\rm op}} \vec{x}_{\rm op}\times i\overline{u}(\vec{0},s')\,\vec{\mathcal{F}}^C\left(\frac{r}{2},-\frac{r}{2},z,x_{\rm op}\right)u(\vec{0},s), \tag{3.27}$$

where $\Sigma_i = \frac{1}{4i}\epsilon_{ijk}[\gamma_j,\gamma_k]$. Here, $i\vec{\mathcal{F}}^C$ represents the quantum-mechanical current, and the above equation resembles the conventional expression for the magnetic moment created by a static, localized current [43]:

$$\vec{\mu} = \frac{1}{2}\int d^3r\,\left[\vec{r}\times\vec{J}(\vec{r})\right]. \tag{3.28}$$

The precise connection between Eqs. (3.27) and (3.28) is worked out in Appendix B.

The optimization introduced in the end of Section 3.3 can also be applied in this calculation. In the summation of Eq. (3.27), we can restrict the sum over z, because of the internal photon vertices are symmetrically treated. This modification can be expressed by the following formula:

$$\begin{aligned}\frac{F_2(0)}{2m_\mu}\overline{u}(\vec{0},s')\,\vec{\Sigma}\,u(\vec{0},s) &= \sum_{r,z,x_{\rm op}} \mathfrak{Z}\left(\frac{r}{2},-\frac{r}{2},z\right)\\ &\quad\cdot\frac{1}{2}\,\vec{x}_{\rm op}\times i\overline{u}(\vec{0},s')\,\vec{\mathcal{F}}^C\left(\frac{r}{2},-\frac{r}{2},z,x_{\rm op}\right)u(\vec{0},s),\end{aligned} \tag{3.29}$$

where the function $\mathfrak{Z}$ encode the z summation region information. It can be defined in the following way:

$$\mathfrak{Z}(x,y,z) = \begin{cases} 3 & \text{if } |x-y|<|x-z| \text{ and } |x-y|<|y-z| \\ 3/2 & \text{if } |x-y|=|x-z|<|y-z| \text{ or } |x-y|=|y-z|<|x-z| \\ 1 & \text{if } |x-y|=|x-z|=|y-z| \\ 0 & \text{otherwise.}\end{cases} \tag{3.30}$$

This trick is used in the calculation presented in Section 4.4 and Section 4.5.

Chapter 4

Numerical Studies

In this section we describe our numerical results. This discussion is divided into five subsections. In the first, Sec. 4.1, we describe the QCD gauge ensembles used in the calculation and explain our treatment of the electromagnetic degrees for freedom, in particular our method for treating the zero or near-zero modes of the photon field in finite volume. We also explain how the form factor $F_2(q^2)$ is determined from the Euclidean-space correlator that we evaluate. Section 4.2, describes a series of example calculations exploring the statistical properties of four techniques that can be used in the calculation of cHLbL, using a stochastic representation for the photon propagator described in Sec. 3.1. In Sec. 4.3, we describe in more detail the use of exact photon propagators whose source points are chosen stochastically, giving both our methods and results, including results for the large 4.6 fm, $32^3 \times 64$ volume and 171 MeV pion mass. In Sec. 4.4 we extend the exact-photon-propagator method, now computing the moment as proposed in Sec. 3.4 and present further $32^3 \times 64$ calculations evaluated at $q^2 = 0$. In addition, We show larger 5.5 fm, $48^3 \times 64$ volume, physical 139 MeV pion mass results, with the same method. In Sec. 4.5, we apply the exact-photon-propagator and moment methods to the calculation of $(g_\mu - 2)$ for the case of the QED light-by-light scattering amplitude, in which the internal loop is a muon instead of a quark, examining the vanishing lattice spacing and large-volume limits. This discussion gives a first indication of

the size of the systematic errors associated with finite volume and finite lattice spacing in our results. It also provides a useful consistency check, since we can compare our result with that known from conventional perturbation theory.

4.1 Computational setup

We have carried out a series of lattice QED and QCD calculations to both develop the methods described in the previous section and obtain a result of the cHLbL contribution to $g_\mu - 2$ using a relatively light pion in large volume. We will now provide some of the details of those calculations. The QCD calculations were performed using four ensembles with the pion masses and lattice volumes listed in Table 4.1. Although each of the ensembles listed in Table 4.1 incorporates 2+1 flavors, with two degenerate, light sea quarks and one physical-mass, strange sea quark, we typically calculate the contribution of a single light quark but multiply by the charge factor $(2/3)^4 + (-1/3)^4 = 17/81$ to obtain the result expected from a mass-degenerate up- and down-quark doublet with charges $+2/3$ and $-1/3$. Most of our results address only this light quark contribution, although for the large-volume, light-pion calculation we also include an explicit, physical strange quark contribution.

The ensembles listed in Table 4.1 were obtained using domain wall fermions (DWF) [46] and the same DWF Dirac operator was used for the quark loop in the cHLbL calculation. However, for the cHLbL calculations on the 32ID ensemble we used a Möbius variant [41] of the DWF operator that was used to generate the ensemble. This Möbius Dirac operator used $L_s = 12$ and Möbius parameters $b + c = 32/12$ and $b - c = 1$, chosen to ensure that the corresponding Möbius DWF quark propagator agrees at the few 0.1% level with the DWF quark propagator used when generating the ensemble. The 48I ensemble was generated with Möbius DWF operator with $b + c = 2$ and $b - c = 1$. All of the quark propagators used the five-dimensional mass $M_5 = 1.8$.

We also use the DWF action for the muon. We compute the muon propagators with

Table 4.1: List of ensembles used in our calculations. Two light and one strange sea quark flavor of domain wall fermions were used when generating these ensembles, where L_s is the length of fifth dimension. The strange quark mass was chosen close to its physical value. The values for Z_V are obtained from Tables XLIII, III, and VI of Refs. [3], [4], and [5] respectively.

Label	Size	L_s	a^{-1}(MeV)	m_π(MeV)	Z_V	Ref
16I	$16^3 \times 32$	16	1747	423	0.6998(20)	[44]
24I	$24^3 \times 64$	16	1747	423	0.6998(20)	[45]
24IL	$24^3 \times 64$	16	1747	333	0.6991(17)	[45]
32ID	$32^3 \times 64$	32	1371	171	0.6685(36)	[4]
48I	$48^3 \times 96$	24	1730	139	0.71076(25)	[5]

the five-dimensional mass $M_5 = 1$ and infinite L_s. Since all the muon-photon interactions have been explicitly included in our formulas, the muon propagators are free fermion propagators. To calculate these free propagators, we use Fourier transformations and analytic expressions [47]. This allows us to exploit the physical properties of DWF with essentially the same computation cost as would be required for fermions without chiral symmetry, *e.g.* Wilson fermions. Because the contribution of those cHLbL subgraphs to $g_\mu - 2$ which contain one or more photon-muon vertices will have a negative degree of divergence, we can use local currents for the photon-muon coupling at x', y', and z' and incur only $O(a^2)$ errors.

As is discussed in detail in Appendix A, we can avoid a divergent contact term resulting from the quark loop in the cHLbL diagram if only one of the four vertices where a photon attaches to that quark loop is given by a conserved current. Thus, we use the complete, five-dimensional, nonlocal conserved form for the external current, while for the three vertices x, y, and z attached to internal photons we use the simpler local, four-dimensional current in the above formulas. We introduce the factor of Z_V^3 that is needed to properly normalize

these three local, nonconserved currents. (The additional convergence provided by the first, position-space moment of the cHLbL amplitude allows us to use only local currents for that case.)

We use Feynman gauge for the photon propagator, which can be written as

$$G_{\mu,\nu}(x,y) = \frac{1}{VT}\sum_{\substack{k \\ |\vec{k}|\neq 0}} \frac{\delta_{\mu,\nu}}{\widetilde{k}^{\,2}} \exp\bigl(ik\cdot(x-y)\bigr), \tag{4.1}$$

where VT is the space-time volume in lattice units. The four-vector $k = (k_0, \vec{k})$ is determined by four integers $k = 2\pi(n_0/T, \vec{n}/L)$, where the integers n_ν, $0 \le \nu \le 3$ obey $-T/2 < n_0 \le T/2$ and $-L/2 < n_i \le L/2$ for $1 \le i \le 3$. The four-vector $\widetilde{k}$ appearing in the denominator of Eq. (4.1) is given by

$$\widetilde{k}_\nu = 2\sin\left(\frac{k_\nu}{2}\right). \tag{4.2}$$

The omission of all Fourier modes with $\vec{k} = 0$ from the sum appearing in Eq. (4.1) removes a possible infrared singularity and will contribute to the finite-volume error that is present in our results [48].

As a first step of generating stochastic photon fields, we define a complex photon field

$$\mathcal{A}_\nu(x) = \frac{1}{\sqrt{VT}}\sum_{\substack{k \\ |\vec{k}|\neq 0}} \frac{\epsilon_\nu(k)}{\sqrt{(\widetilde{k})^2}} \exp(ik\cdot x), \tag{4.3}$$

where $\epsilon_\nu(k)$ is a random complex variable which satisfies

$$\langle \epsilon_\mu(k)\epsilon^*_\nu(k')\rangle_A = \delta_{\mu,\nu}\delta_{k,k'}, \tag{4.4}$$

$$\langle \epsilon_\mu(k)\epsilon_\nu(k')\rangle_A = 0, \tag{4.5}$$

and the average $\langle\ldots\rangle_A$ indicates an average over the random variables $\epsilon_\nu(k)$. In our calculations, we choose $\epsilon_\nu(k)$ to be a Gaussian random variable, which is similar to the distribution of the gauge fields found in conventional QED gauge ensembles. We can verify that this

complex stochastic field will generate the desired Feynman-gauge photon propagator:

$$\langle \mathcal{A}_\mu(x)\mathcal{A}^*_\nu(y)\rangle_A = \frac{1}{VT}\sum_{\substack{k\\ |\vec{k}|\neq 0}}\sum_{\substack{k'\\ |\vec{k}'|\neq 0}} \left\langle \epsilon_\mu(k)\epsilon^*_\nu(k')\right\rangle_A \frac{e^{ik\cdot x}}{\sqrt{(\widetilde{k})^2}}\frac{e^{-ik'\cdot y}}{\sqrt{(\widetilde{k}')^2}} \tag{4.6}$$

$$= G_{\mu,\nu}(x,y). \tag{4.7}$$

Finally a real stochastic photon field can be constructed from the real part of $\mathcal{A}_\mu(x)$:

$$A_\mu(x) = \sqrt{2}\,\mathrm{Re}\,\mathcal{A}_\mu(x), \tag{4.8}$$

which obeys

$$\langle A_\mu(x)A_\nu(y)\rangle_A = \frac{1}{2}(\langle \mathcal{A}_\mu(x)\mathcal{A}^*_\nu(y)\rangle_A + \langle \mathcal{A}^*_\mu(x)\mathcal{A}_\nu(y)\rangle_A) = G_{\mu,\nu}(x,y). \tag{4.9}$$

It is this real stochastic photon field $A_\mu(x)$ that we use in the calculation.

While the three-momenta of the initial and final muons are typically fixed to be $\pm\vec{q}/2$, we calculate all 16 amplitudes corresponding to all possible initial and final spinor indices, α and β. We extract the form factor $F_2(q^2)$ from the resulting 4×4 matrices $\mathcal{M}_\nu(\vec{q})_{\alpha\beta}$ for different external photon polarizations ν of Eq. (3.2) by matching to the Green's function shown in Fig. 4.1. This diagram represents the result of a tree-level calculation with a muon source and sink identical to those used in our lattice calculation, but with a vertex function that is expressed in terms of the general invariant functions $F_1(q^2)$ and $F_2(q^2)$ using Eq. (3.1).

Figure 4.1: The shaded circle represents the vertex $F_1(q^2)\gamma_\nu + i\frac{F_2(q^2)}{4m_\mu}[\gamma_\nu,\gamma_\beta]q_\beta$.

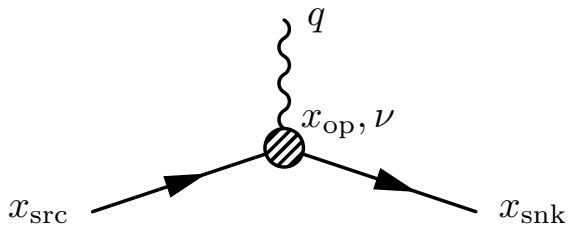

We compute the tree-level amplitude $(\mathcal{M}^{\mathrm{tree}}_\nu(\vec{q}))_{\alpha\beta}$ described by the diagram given in Fig. 4.1 as a function of the input variables $F_1(q^2)$ and $F_2(q^2)$ on the same lattice volume,

with the same muon source and sink momenta as were used in the cHLbL calculation, obtaining

$$\mathcal{M}_\nu^{\text{tree}}(\vec{q}) = e^{E_{q/2}(t_{\text{snk}}-t_{\text{src}})} e^{i\vec{q}\cdot\vec{x}_{\text{op}}} \sum_{\vec{x}_{\text{snk}},\vec{x}_{\text{src}}} e^{-i\frac{\vec{q}}{2}\cdot(\vec{x}_{\text{snk}}+\vec{x}_{\text{src}})} \cdot S_\mu(x_{\text{snk}}, x_{\text{op}}) \Big(F_1(q^2)\gamma_\nu + i\frac{F_2(q^2)}{4m_\mu}[\gamma_\nu,\gamma_\beta]q_\beta \Big) S_\mu(x_{\text{op}}, x_{\text{src}}). \tag{4.10}$$

We then find the two values of $F_1(q^2)$ and $F_2(q^2)$ that minimize the difference

$$\sum_\nu \sum_{\alpha,\beta} \left| \Big(\mathcal{M}_\nu(\vec{q})\Big)_{\alpha\beta} - \Big(\mathcal{M}_\nu^{\text{tree}}(\vec{q})\Big)_{\alpha\beta} \right|^2. \tag{4.11}$$

In most of our simulations, we choose $\vec{q}$ to be in the z direction. Since $(\mathcal{M}_z^{\text{tree}}(\vec{q}))_{\alpha\beta}$ will then naturally be zero, we omit that direction from the above summation.

In the moment method, both muons carry zero momentum and the resulting, simplified spinor structure is given in Eq. (3.27). Because $F_1(0) = 0$ in this case, we only need to find the minimum with respect to $F_2(0)$ and can neglect the amplitude $(\mathcal{M}_t(\vec{q}))_{\alpha\beta}$ corresponding to polarization in the t direction. However, we still evaluate the tree diagram of Fig. 4.1 and minimize the expression in Eq. (4.11) to obtain $F_2(0)$.

When computing quark propagators on configurations belonging to the four ensembles described in Table 4.1, we use low-mode deflation with 100 eigenvectors for the 16I ensemble and 550 eigenvectors for the other three ensembles. These low modes are also used when computing the reduced-precision propagators that are used in the all-mode-averaging procedure described below. Except for these low-precision inversions, the Dirac operator was inverted using a stopping condition of 10^{-8}. More specifically, we required that the inverse of a product of the preconditioned Dirac operator times its Hermitian conjugate solve the Dirac equation with a residual whose norm was 10^{-8} times smaller than the norm of the vector to which the inverse was applied.

We conclude this subsection with a discussion of the unconventional strategy which we have implemented in all of the numerical work presented here. In contrast to most lattice

QCD calculations, the initial and final states do not contain quarks and enter a computationally inexpensive portion of the calculation. The bulk of the computational effort is associated with evaluating quark propagators whose sources have fixed positions in space-time and are necessarily located close to the position $x_{\rm op}$ of the external current J_ν. In order to suppress the contribution of excited states (typically states of a muon with one or more photons) we must work with large time separations $t_f - t_{\rm op}$ and $t_{\rm op} - t_i$. To the extent that these separations are large, our final Green's functions will depend on t_f and t_i only through their difference $t_f - t_i$, which we hold fixed at $T/2$. In order to achieve the greatest suppression of excited states, we will choose the locations of the muon source and sink to be maximally distant from the sources of the quark propagators. Specifically, we locate t_f and t_i so that the average $w = (x + y)/2$ appearing in Eq. (3.11) lies midway between t_f and t_i. This means that we do not keep $t_f - t_{\rm op}$ and $t_{\rm op} - t_i$ fixed but instead average over a range of large values of $t_f - t_{\rm op}$ and $t_{\rm op} - t_i$, upon which the quantity we are computing should not depend. In order to provide numerical evidence that the effects of excited states have been reduced below the level of our statistical errors, we simply vary $t_{\rm sep} = t_f - t_i$ to explore the degree to which our results depend on it.

4.2 Example stochastic photon calculations

In Sec. 3.1 we compared the original subtraction method used to obtain the first lattice QCD results for $g_\mu - 2$ [8] and an alternative stochastic method in which specific random photon fields are introduced to construct only the three propagators needed for the $O(\alpha^3)$ cHLbL amplitudes. In this section, we will not attempt a numerical comparison of these two methods, since the absence of both $O(\alpha^2)$ noise and the need to remove unwanted $O(\alpha^4)$ and higher-order terms gives the latter method a clear advantage. (A comparison of the original method and a combination of many of the improvements suggested in this thesis can be found in Fig. 4.5, presented later in this section.) Instead we will begin by comparing a

series of variations of the stochastic field method.

Table 4.2: Results for F_2 evaluated at $q^2 = (2\pi/L)^2$ for three stochastic propagator methods. The calculations were performed on a $16^3 \times 64$ lattice with a muon mass of 0.02, a time separation of 32 between the muon source and sink and using an internal muon loop. For this test we used a local current for the external photon and conserved currents for internal photons. However, the 2- and 3-photon contact terms needed for these conserved currents were not included. A summary of these results has been presented in Ref. [6].

Method	$F_2/(\alpha/\pi)^3$	N_{prop}	$\sqrt{\text{Var}}$	N_{sample}	$\sqrt{\text{Var}_{\text{Eff}}}$
Stoch.	0.2228(46)	$9,864 \times (2 \times (1+12))$	2.3	$9,864 \times 12^2$	5.5
Stoch. w/o M^2	0.1962(368)	$18,432 \times (2 \times (1+1))$	10.0	$18,432 \times 1^2$	5.0
Stoch. ext. pt.	0.232(33)	$18,096 \times (2 \times (1+6))$	16.6	$18,096 \times 6^2$	28.4

4.2.1 M^2 method

We first study the statistical advantage that results if we compute M sequential-source propagators for the x vertex in Fig. 3.1 with momentum $-q/2$ injected at the external current vertex and an additional M sequential-source propagators for the y vertex with the momentum $+q/2$ injected, and then evaluate all M^2 possible pairs. This test is carried out on a $16^3 \times 64$ lattice and uses muon propagators for both the external muon and the internal loop. Thus, there are no fluctuating QCD configurations, and the resulting statistical noise comes entirely from the stochastic photon propagators.

The advantage of using the M^2 method can be seen by comparing the first two rows of Table 4.2. The first row evaluates $M = 12$ stochastic propagators for each of the two sequential-sources created from propagators whose sources correspond to the external current with four-momenta $+q/2$ and $-q/2$ and combines them using all M^2 possible pairs.

The second row uses two stochastic sequential-source propagators corresponding to single sequential-sources at the x and y vertices in Fig. 3.1, again carrying the momenta $\pm q/2$. Both the first and second rows of Table 4.2 use a random space-time volume source for the external current. The quantity N_{prop} listed in the third column in Table 4.2 is the total number of propagator inversions required for each result and is given by

$$N_{\text{prop}} = N_{\text{ext-cur}}\big(2(1+M)\big). \tag{4.12}$$

Here the factor $1+M$ corresponds to 1 random wall- (or point-) source inversion and M sequential-source inversions for M different stochastic photon fields, while $N_{\text{ext-cur}}$ is the number of random wall or point sources used for the external current. The extra factor of 2 is needed because the external photon carries momentum, which requires two separate momenta for the fermions entering and exiting at this vertex.

As can be seen from the first two rows of Table 4.2, we realize a substantial reduction in statistical error when using the M^2 method. Since the computational cost involved in these two rows is not the same, a precise comparison requires more than a simple comparison of the resulting statistical errors. This comparison is assisted by the $\sqrt{\text{Var}}$ and $\sqrt{\text{Var}_{\text{Eff}}}$ columns in that table. In each of these columns, we begin with the quoted jackknife statistical error and compute a measure of the width of distribution of individual samples before the average over samples is performed. For the quantity $\sqrt{\text{Var}} = \text{Err}\sqrt{N_{\text{prop}}}$, we simply expand the final error (Err) by a factor given by the square root of the number of internal loop propagators that were computed to produce that error. The comparison of $\sqrt{\text{Var}}$ between the first and second rows suggests that the statistical fluctuations found in the result for a given computational cost were roughly 5 times smaller for the M^2 method. The quantity $\sqrt{\text{Var}_{\text{Eff}}} = \text{Err}\sqrt{N_{\text{sample}}}$, where $N_{\text{sample}} = N_{\text{ext-cur}}M^2$ inflates the final quoted error by the square root of the number of "effective" samples N_{sample}, which in this case treats the M^2 samples as if they were all independent. Here the resulting nearly equal "effective" variances imply that this hypothesis is true and these M^2 samples are essentially independent. Thus,

if only the cost of the internal muon line is considered, in this case the M^2 method has reduced the computational cost by a factor of $M = 12$.

The choice of $M = 12$ made in this test was motivated by the case of QCD with an internal quark loop. In that case the M^2 method allows M^2 samples from $2M$ computationally expensive light quark propagator inversions. However, we need to evaluate the product of external muon propagators for all six different permutations of the three internal photons, each pair of stochastic photons joined to x and y and all combinations of photon polarizations. Since this muonic part of the calculation grows at M^2 we cannot make M too large. In our simulations, the choice $M = 12$ balances the cost of muons and quarks but is not so large that the QCD gauge noise seen from configuration to configuration dominates the statistical noise, so the statistical gain is still proportional to M^2.

4.2.2 Random wall sources for the external current

A second, standard method to increase the efficiency of this cHLbL calculation attempts to increase the degree of volume averaging by using a random wall source for the two sequential-source propagators appearing in the internal loop, instead of choosing one or more point sources. For a random source at a given time t_{op} we use a full spatial vector of Gaussian random numbers, with a different vector being chosen for each spin and color. As described above, two independent noise vectors are needed with momentum factors $\exp(\pm iq \cdot x_{\text{op}}/2)$. If the propagators corresponding to one of these two noise sources are multiplied by the complex conjugate of the other, which are then combined with the second noise vector and the complex conjugate of the first, an expression can be constructed whose noise average will be the desired sum over all locations of $\vec{x}_{\text{op}}$ for a fixed choice of t_{op}. Such random volume sources were used to obtain the results given in the first two rows of Table 4.2.

In order to determine the value of this use of a random wall source, we generated the results in the third row of Table 4.2 by using $N_{\text{ext-cur}}$ point-source locations for the external

current. (Here the extra factor of 2 in cost for external current sources carrying the momenta $\pm q/2$ could have been avoided, but this would not have changed the qualitative conclusion.) By comparing the first and third rows of Table 4.2, one sees a 5- to 8-times reduction in the errors from the use of a random wall source.

4.2.3 Breit-frame muon momenta

The symmetrical choice of $\pm\pi/L$ for the outgoing and incoming momentum has aesthetic appeal and only nonzero spatial momenta as is required for a direct lattice measurement of a magnetic moment. However, by avoiding assigning a $2\times$ larger spatial momentum of $2\pi/L$, this approach also results in substantially smaller statistical errors than the simpler assignment of the allowed finite-volume four-momenta $(m_\mu, \vec{0})$ and $(\sqrt{m_\mu^2 + (2\pi/L)^2}, 2\pi/L\hat{e})$ to the incoming and outgoing muon momenta. The errors obtained using this standard assignment and those resulting from the Breit- or brick-wall-frame choice made here, with the incoming and outgoing four-momenta $(\sqrt{m_\mu^2 + (\pi/L)^2}, \mp\pi/L\hat{e})$ are compared in Table 4.3. (Here $\hat{e}$ is a unit vector in the direction of one of the three spatial axes.) This comparison is identical to that shown in Table 4.2 except the muon mass has been reduced from 0.02 to 0.01 and shows an approximate 15-times reduction in error, which is equivalent to what would be obtained with 200 times the statistics. Such a reduction in error should be expected. When the initial and final momenta are $\vec{q}$ and $\vec{0}$, the signal behaves as $\exp(-(E_{\vec{q}} + E_{\vec{0}})t_{\text{sep}}/2)$. However, the noise behaves as $\exp(-E_{\vec{0}}t_{\text{sep}})$, which leads to an exponentially decreasing signal-to-noise ratio in the large-time-separation limit.

Table 4.3: Comparison of results obtained with muon momenta of $\pm q/2\hat{e}$ using twisted boundary conditions for the initial and final muon propagators and those obtained when the initial muon carries zero momentum and the final muon is given $q\hat{e}$. Here $q = 2\pi/L$, and $\hat{e}$ is a unit vector parallel to one of the edges of the spatial volume. Except for the choice of muon mass, $m_\mu = 0.01$, all features of the calculation and definitions are the same as those for Table 4.2. A summary of these results has been presented in Ref. [6].

Method	$F_2/(\alpha/\pi)^3$	$N_{\rm prop}$	$\sqrt{\rm Var}$	$N_{\rm sample}$	$\sqrt{\rm Var_{Eff}}$
Stoch. $\vec{p}_1 = -\frac{\pi}{L}\hat{e}$	0.1666(69)	$1584 \times (2 \times (1 + 12))$	1.4	1584×12^2	3.3
Stoch. $\vec{p}_1 = \vec{0}$	0.2278(265)	$10260 \times (2 \times (1 + 24))$	19.0	10260×24^2	64.4

4.3 Exact photon propagators

The use of exact instead of stochastic photon propagators is the most significant improvement in method suggested in this thesis because of its elimination of stochastic noise which grows with the volume. In this subsection we describe the implementation of this method, compare it with our earlier results, and apply it to obtain the cHLbL contribution to $g_\mu - 2$ for the near-physical circumstance with $m_\pi = 171$ MeV and a reasonably large $32^3 \times 64$ lattice volume which is 4.6 fm on a side in physical units.

As described earlier, we choose stochastically the location of two of the three vertices x and y at which the internal photons couple to the quark loop. The pair of positions x and y are point sources for the quark propagators, and we arrange the contractions so that the location of the external current, $x_{\rm op}$, and the third photon vertex, z, appear as sinks and are explicitly summed over space-time. While computational cost prevents our performing an explicit sum over all space-time separations $r_\nu = x_\nu - y_\nu$, we can split the computation of

the sum into two parts. The first part contains all r_ν values with Euclidean magnitude less than a certain value: $|r| \leq r_{\max}$. Here we evaluate all distinct separations r_ν up to discrete symmetries. The second part of the sum, where the magnitude $|r|$ is larger than $r_{\max}$, is evaluated by averaging over random point-pair samples, weighted to increase the sampling efficiency.

Table 4.4: Comparison of the stochastic and exact photon methods carried out on the 16I ensemble with $m_\mu = 332$MeV and the separation between the muon source and sink $t_{\text{sep}} = 16$. As in the previous tables $\sqrt{\text{Var}} = \text{Err}\sqrt{N_{\text{confs}} N_{\text{prop}}}$. Here N_{confs} is the number of configurations analyzed and N_{props} the number of propagators that are computed on each configuration. In both cases $F_2(q^2)$ is evaluated at the minimum, nonzero lattice momentum transfer $(2\pi/L)^2$.

Method	$F_2/(\alpha/\pi)^3$	N_{confs}	N_{prop}	$\sqrt{\text{Var}}$
Stoch.	0.1485(116)	31	$32 \times (2 \times (1 + 6))$	1.37
Exact	0.1235(26)	16	$129 + 16 \times 16$	0.051

We compare the exact-photon method with our previous stochastic method by performing a test on the 16I ensemble. The results are listed in Table 4.4. For the stochastic method, the total number of propagator inversions per configuration, $N_{\text{props}} = N_{\text{set}}\big(2(1 + M)\big)$ where $1 + M$ corresponds to 1 random wall-source inversion and M sequential-source inversions for M different stochastic photon fields. The quantity N_{set} is the product of the number of random sources used per time slice and the number of time slices used on each configuration analyzed. For the exact-photon method, $N_{\text{props}} = N_{\text{short-dist}} + N_{\text{set}} M$. In the "stochastic" method, we use a local current for the external photon and the conserved current for the internal photons, with the necessary contact terms included in these cases. In the "exact-photon" method, we use the conserved current for the external photon and a local current

Table 4.5: The magnetic form factor $F_2(q^2)$ evaluated at $q^2 = (2\pi/L)^2$ for our four ensembles. In each case, we choose the muon mass to give the physical value for ratio of muon to pion mass. The 32ID-S results are obtained from the 32ID ensemble but with the loop mass set to that of the strange instead of the light quark. The actual strange quark contribution to cHLbL for the 32ID ensemble would be the value shown divided by 17 to introduce the proper electric charge weighting. The last two lines are for comparison: "Model" is the result presented at the Glasgow meeting [7] and " Exp − SM" is the E821 experimental value minus the standard model prediction, without a HLbL contribution.

Label	m_μ/MeV	N_{confs}	$F_2/(\alpha/\pi)^3$
16I	332	16	0.1235(26)
24I	332	17	0.2186(83)
24IL	261	18	0.1570(69)
32ID	134	47	0.0693(218)
32ID-S	134	23	0.0195(88)
Model			0.08(2)
Exp − SM			0.28(7)

for each internal photon coupling. (There are no contact terms required in this case.) We can see that even on this relatively small volume the exact-photon method is more than 700 times as cost effective as the stochastic method.

The results for $F_2(q^2)$ at $q^2 = (2\pi/L)^2$ using the exact-photon method for each of the ensembles listed in Table 4.1 are presented in Table 4.5. The statistical weights for the separations between the pairs and other simulation parameters used to obtain these results are listed in Table 4.6.

Since we calculate the contribution for each x-y pair, the results contain more information

Table 4.6: Simulation parameters used to obtain the results given in Table 4.5. The quantity $r_{\max}$ is the upper bound on the magnitude of the $x-y$ separations which are evaluated without random sampling, M is the number of randomly sampled points that are combined using the M^2 method, while N_{set} is the number of groups of these M samples analyzed per QCD configuration. Note, for each set of M random points we randomly chose a point s in the lattice volume and then the M stochastic points which will be used for the vertices x and y are chosen relative to that random point s following the weight $p(x-s)$.

Label	$r_{\max}$	$p(x)$	M	N_{set}	$\frac{\text{Cost per conf}}{\text{BG/Q rack days}}$
16I	4	$1/\lvert x\rvert^{3.5}$	16	16	0.039
24I	4	$1/\lvert x\rvert^{3.5}$	16	16	0.178
24IL	4	$1/\lvert x\rvert^{3.5}$	16	16	0.177
32ID	3	$1/\lvert x\rvert^{3.5}$	16	8	0.224
32ID-S	4	$1/\lvert x\rvert^{4}$	8	8	0.085

than a single final number. In Fig. 4.2, we plot a histogram of the contributions to F_2 from different point-pair separations and a scatter plot of the F_2 contribution from each random point-pair sample. Shown are results for the four different QCD ensembles described in Table 4.1. The fifth row labeled 32ID-S uses the strange instead of the light quark in the quark loop, evaluated on the 32ID ensemble. Table 4.6 lists the choices made in sampling the points x and y for each case. As can be seen in Fig. 4.3, the majority of the contribution to F_2 comes from a separation of $|r| \leq 10$ in lattice units or $|r| \leq 1.4$ fm. However, most of the statistical noise comes from the more difficult to sample, larger separations with $|r| \geq 1.4$ fm, even for the case of the heavier strange quark.

We conclude the discussion of the exact propagator method at nonzero q^2 by examining two of the possible enhancements. The first involves including two extra diagrams so that the external current is conserved on each configuration as was discussed in Sec. 3.3. The second can be viewed as an adaptation of the M^2 method discussed for the case of stochastic fields in Sec. 4.2.1 to the exact propagator case. In the present case we compute the needed sequential-source quark propagators from M locations of the point x and then evaluate the contribution to F_2 from each of the $M(M-1)/2$ distinct pairs that can be formed from this set of M points.

4.3.1 Conserved current on each configuration

We repeated the 32ID lattice computation with the same parameter choices but included all three diagrams in Fig. 3.3 in order to determine the value of this potential enhancement, described in Sec. 3.3. The results are listed in Table 4.7 as the "conserved" method. We find that although the cost per stochastic point is 7 times larger than for the case that only one diagram is evaluated, this extra cost yields a marginal overall benefit in the reduction of noise.

Figure 4.2: The left column shows histograms of the contribution to F_2 from different separations $|r| = |x - y|$. The sum of all these points gives the final result for F_2. The right column contains scatter plots of results for F_2 for all random point pairs, adjusted by their sampling weight. The average value of F_2 from all points gives the $|r| \geq r_{\max}$ portion of the final result. The vertical lines in the left plots and the left-hand boundaries of the right plots indicate the value of $r_{\max}$. The labels 16I, 24I, 24IL and 32ID indicate the ensembles given in Table 4.1.

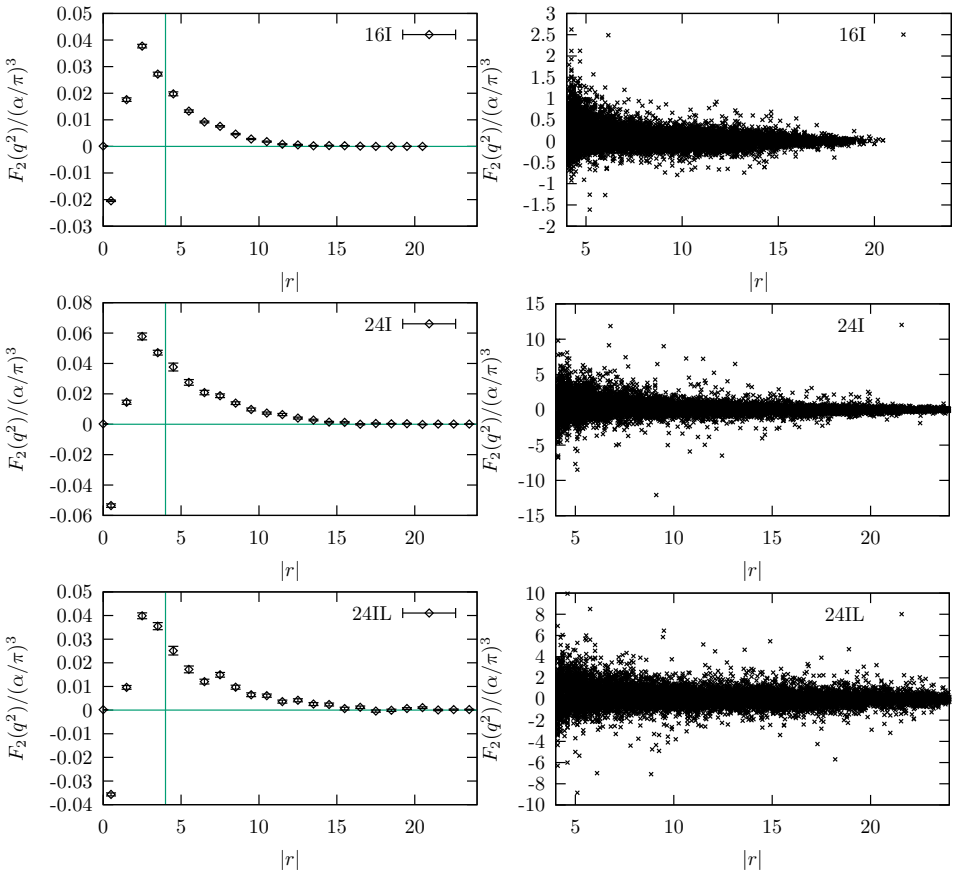

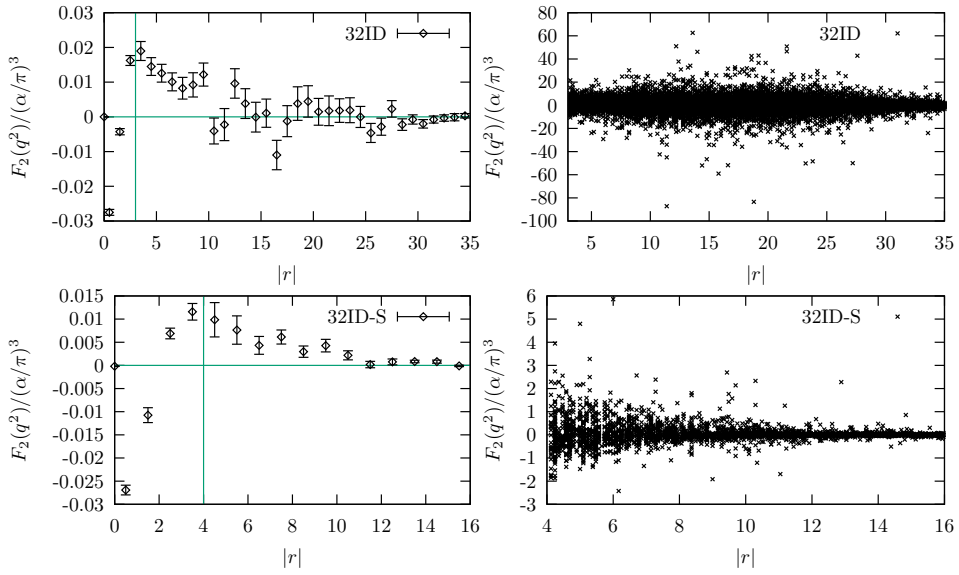

4.3.2 M^2 method

We can analyze the effectiveness of this M^2 method for exact photon propagators by comparing two different methods of estimating the statistical error that results from the long-distance contribution to F_2 coming from point pairs with $r \geq r_{\max}$. In Table 4.7, we list separately the results and errors from the short- and long-distance parts. The errors are correct statistical errors computed from the variance of the average values obtained for each configuration. However, we can also estimate a second long-distance error, denoted as "ind-pair" in the table, by assuming that the long-distance point pairs are all completely independent even though on a given configuration they are simply different combinations of the same set of points. If the correlations between these point pairs are significant, we should expect that the error obtained by treating them as independent and dividing the width of the distribution of results from these pairs by $\sqrt{N_{\text{set}} N_{\text{conf}} M(M-1)/2}$, will be less than the true error, determined by the first method described above. From the table we can see that the error found by treating these $M(M-1)/2$ pairs as independent is only slightly smaller than the actual error, which suggests a significant gain from evaluating the contribution of these $M(M-1)/2$ pairs. Once again we see an $O(M^2)$ statistical advantage

from the calculation of only $O(M)$ propagators.

4.4 Moment method

Here we present results that are obtained by using the best of the strategies discussed in Chapter 3. Specifically, we evaluate $F_2(q^2)$ at the point of interest $q^2 = 0$ using the moment method of Sec. 3.4. We also introduce the restriction $|z - x| \geq |x - y|$ and $|z - y| \geq |x - y|$ explained at the end of Sec. 3.3 in order to more accurately sample the region where one of the three vertices is far from the other two. We use the 32ID and 48I ensemble lattices and increase the efficiency of the calculation by using the all-mode-averaging (AMA) method [28, 29], in which most of the propagator inversions are computed imprecisely and a small but more computationally expensive correction term is computed far less frequently.

For 32ID ensemble, we compute the short-distance part up to $r_{\max} = 5$ with the following samplings: We compute point pairs with $|r| \leq 1$ six times, $1 < |r| \leq 2$ five times, $2 < |r| \leq 3$ four times, $3 < |r| \leq 4$ two times, and $4 < |r| \leq 5$ one time for each configuration. We use Eq. (3.27) in this computation and make use of its invariance under a larger set of discrete symmetries, including independent inversions of x, y, z, t, and the exchange of the x, y and z directions.

For the long-distance part, we compute 512 pairs per configuration. In order to more precisely control the distributions of these long-distance $r > 5$, point pairs, we do not use the M^2 method in this calculation and instead choose the individual pairs so that their separation r follows the probability distribution

$$P_{32\mathrm{ID}}(r) \quad \propto \quad \frac{1}{|r|^4} e^{-0.05|r|}. \tag{4.13}$$

The approximate AMA results are computed using propagators that were obtained using only 100 conjugate gradient (CG) iterations. We treat the AMA correction as a separate computation on the same set of configurations. For the short-distance part, we sum the

contribution of the point pairs up to $r_{\max} = 2$. We compute 48 long-distance point pairs per configuration, using the same pair-separation distribution given in Eq. (4.15) for the long-distance part of the AMA correction, but with $|r| > 2$. On this restricted sample we compute the result from propagators computed using only 100 CG iterations and propagators computed with a residual of 10^{-8}.

Table 4.7: Results from three variants of the exact photon method obtained from the 32ID ensemble. The first row, labeled "Exact", corresponds to the row labeled 32ID in Table 4.5. The second row, labeled "Conserved" is similar except all three arrangements of the vertices x, y and z are combined insuring that the external current is conserved on each configuration. The final three rows are obtained from the moment method and are explained in the text.

Method	$F_2/(\alpha/\pi)^3$	N_{conf}	N_{prop}	$\sqrt{\text{Var}}$
Exact	0.0693(218)	47	$58 + 8 \times 16$	2.04
Conserved	0.1022(137)	13	$(58 + 8 \times 16) \times 7$	1.78
Mom. (approx)	0.0994(29)	23	$(217 + 512) \times 2 \times 4$	1.08
Mom. (corr)	0.0060(43)	23	$(10 + 48) \times 2 \times 4$	0.44
Mom. (tot)	0.1054(54)	23		

Method	$r_{\max}$	SD	LD	ind-pair
Exact	3	−0.0152(17)	0.0845(218)	0.0186
Conserved	3	0.0637(34)	0.0385(114)	0.0093
Mom. (approx)	5	0.0791(18)	0.0203(26)	0.0028
Mom. (corr)	2	0.0024(6)	0.0036(44)	0.0045

The results are presented in the final three rows of Table 4.7. We use $m_\mu = 134$ MeV

Figure 4.3: Histograms and scatter plots for the contribution to F_2 from different separations $|r| = |x-y|$ are shown in the left and right plots, respectively, following the conventions used in similar previous figures. The upper two plots are obtained using the conserved version of the exact-photon method on the 32ID ensemble. The lower two plots are obtained using the moment method, but from approximate propagators each obtained from 100 CG iterations, again on the 32ID ensemble.

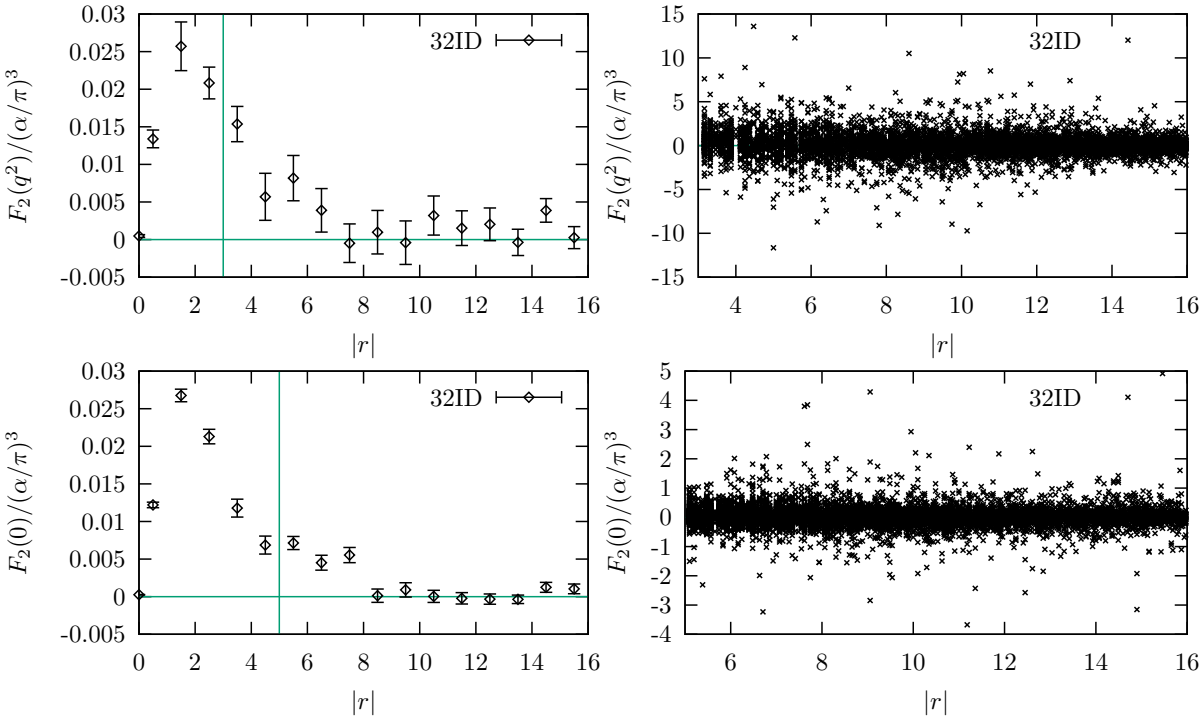

and a separation between the muon source and sink of $t_{\rm sep} = 32$. As in previous tables $\sqrt{\rm Var} = {\rm Err}\sqrt{N_{\rm conf} N_{\rm prop}}$ where the number of propagators computed per configuration, $N_{\rm prop}$, is defined as before. In the moment method, for each point we compute one point source propagator and three sequential-source propagators for each of the three spatial magnetic moment directions. Since the $\sqrt{\rm Var}$ is based on the number of propagators computed, the reduction in $\sqrt{\rm Var}$ seen between the "Conserved" and "Mom. (aprox)" rows of Table 4.7 suggest that we get 40% speed-up from the moment method in addition to the gain in inversion speed that results from using the AMA approach. Although we limit the approximate CG inversions to only 100 iterations, compared with precise inversions which require ~ 1300 iterations, the correction is very small. However, the variance of the correction is rather large, suggesting that the choice of 100 approximate iterations may not be optimum.

In the results presented in Table 4.7 we use local currents for the internal photons. In the "Exact" and "Conserved" methods, we use the conserved current for the external photon, while in the moment method, we use a local current for the external photon. The final row of Table 4.7, labeled "Mom. (tot)," gives the complete result from the moment method, while the preceding two rows, "Mom. (approx)" and "Mom. (corr)," show separately the approximate AMA results and the needed correction term. The "SD" and "LD" columns give the results from the pairs with $|r| \leq r_{\rm max}$ and $|r| > r_{\rm max}$, respectively. The "ind-pair" column gives the error that would be expected if the long-distance pairs were truly independent. Note that the quantity $F_2(q^2)$ is computed at $q^2 = (2\pi/L)^2$ for the first two rows and at $q^2 = 0$ for the final three rows. The final error shown for the moment method on the fifth line of Table 4.7 is obtained by applying the jackknife method to the sum of the approximate AMA result and the AMA correction term. The resulting error is similar to what would be found if the statistical error on the approximate and correction terms were computed separately and added in quadrature.

More information about the conserved and moment method calculations presented in

Table 4.7 can be found in Fig. 4.3, where histograms and scatter plots are presented as functions of the separation of the two stochastically chosen points x and y.

The calculation on 48I ensemble is performed on 69 configurations, each separated by 20 MD time unit. For each configuration, we compute the short-distance part up to $r_{\max} = 5$ with the following samplings: We compute point pairs with $|r| \leq 2$ two times, $2 < |r| \leq 5$ one time for each configuration, also taking discrete symmetries into account. In the long-distance region, we compute 256 pairs per configuration. Their separation r is limited to be more than 5 but less or equal to 24 follows the probability distribution

$$P_{48\mathrm{I}}(r) \quad \propto \quad \frac{1}{|r|^4} e^{-0.01|r|}. \tag{4.14}$$

The approximate AMA results are computed using propagators that were obtained using only 200 single precision conjugate gradient (CG) iterations accelerated with 2000 low modes obtained with Lanczos. To reduce the memory usage of the low modes and reduce the computational cost to multiply the Dirac operator, we adopt zMöbius DWF operator with $L_s = 10$. The zMöbius operators are Möbius operator with complex, s dependent $b(s)$ and $c(s)$. We choose $b(s)$, $c(s)$ to best approximate $L_s = 24$, $b + c = 2$, $b - c = 1$ Möbius DWF operator. Their values used in our calculation are listed in Table 4.8.

Again, we treat the AMA correction as a separate computation on the same set of configurations. We did a two stage AMA in this case. First, we compute 12 point pairs with the same accuracy described above. Then, for the same set of 12 point pairs, we perform the calculation with quite accurate zMöbius DWF inversion which take 400 single precision CG iterations including a defect correction step after the first 200 iterations. The separations of the 12 pairs are only required to be less or equal to 24, and are sampled based on the following distribution

$$P_{48\mathrm{I,c}}(r) \quad \propto \quad \frac{1}{|r|^2} e^{-0.07|r|}. \tag{4.15}$$

For the second stage, we choose 4 pairs among above 12 pairs, and compute them with

Table 4.8: $b(s)$ used in zMöbius operator for 48I calcuation. $c(s) = b(s) - 1$.

s	$b(s)$
0	0.8429203836815970
1	0.9228997923828018
2	1.1017200769981794
3	1.4219097980542994
4	1.9620523417564424
5	2.8654191667525488
6	4.4659153528626341
7	5.5498080139636414
8	$4.9320961582039766 - 3.5559998543638791i$
9	$4.9320961582039766 + 3.5559998543638791i$

residual of 10^{-8} with original Möbius DWF operator. The inversion is also accelerated using the MADWF algorithm [49], benefited from the 2000 low modes and reduced L_s.

The results are presented in the final three rows of Table 4.9. The muon mass $m_\mu =$ 106 MeV used in the calculation is also physical. The separation between the muon source and sink is set to to $t_{\rm sep} = 48$. As in previous tables $\sqrt{\rm Var} = {\rm Err}\sqrt{N_{\rm conf}N_{\rm prop}}$ where the number of propagators computed per configuration, $N_{\rm prop}$, is defined as before. The settings are similar to moment method calculation for 32ID ensemble. Although we limit the approximate CG inversions to only 200 iterations with cheap $L_s = 10$ zMöbius DWF operator, the correction turned out to be small. The AMA setup is successful.

Table 4.9: Results from the moment method obtained from the 48I ensemble.

Method	$F_2/(\alpha/\pi)^3$	$N_{\rm conf}$	$N_{\rm prop}$	$\sqrt{\rm Var}$
Mom. (approx)	0.0951(75)	69	$(112+256)\times 2\times 4$	3.39
Mom. (corr1)	−0.0019(11)	69	$(0+12)\times 2\times 4$	0.09
Mom. (corr2)	0.0001(12)	69	$(0+4)\times 2\times 4$	0.06
Mom. (tot)	0.0933(73)	69		

Method	$r_{\rm max}$	SD	LD	ind-pair
Mom. (approx)	5	0.0763(21)	0.0188(73)	0.0079
Mom. (corr1)			-0.0019(11)	0.0015
Mom. (corr2)			0.0001(12)	0.0014

We should emphasize that the moment-method result given in the final line of Table 4.9 is the most important numerical result presented in this thesis. It provides the cHLbL contribution (calculated directly at $q^2 = 0$) to $g-2$ for the muon with a 8% statistical

Figure 4.4: Histograms and scatter plots for the contribution to F_2 from different separations $|r| = |x - y|$ are shown in the left and right plots, respectively, following the conventions used in similar previous figures. The two plots are obtained using the moment method, but from approximate propagators each obtained from 200 CG iterations on the 48I ensemble.

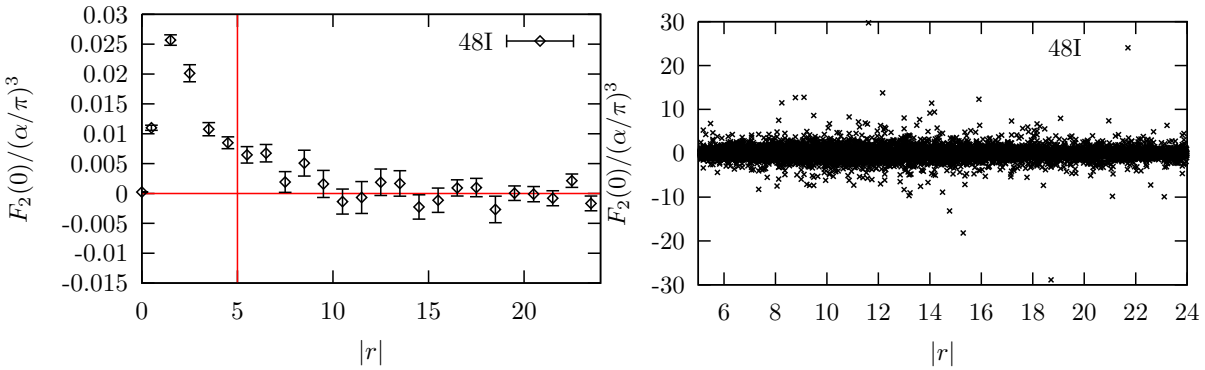

accuracy for the case of a pion with $m_\pi = 139$ MeV using a $(5.5\text{ fm})^3$ spatial volume, but with a relatively coarse lattice spacing a with $1/a = 1.73$ GeV. More information about the conserved and moment method calculations presented in Table 4.9 can be found in Fig. 4.4, where histograms and scatter plots are presented as functions of the separation of the two stochastically chosen points x and y.

As a final topic in this section, we apply the conserved method and the moment method, with the restriction $|z - x| \geq |x - y|$ and $|z - y| \geq |x - y|$ that was described previously, to the 24I ensemble with $m_\mu a = 0.1$ in order to compare these methods with the original subtraction calculation [8] which was carried out on the same ensemble with the same muon mass. We compute the short-distance part up to $r_{\max} = 4$. For $|r| \leq 2$ we compute each independent direction twice, while for $2 < |r| \leq 4$ each independent direction is computed only once for each configuration. We take many discrete symmetries into account when summing over the short-distance part, including independent inversions of x, y, z, t, and exchanges of the x and y directions. For the long-distance part, we do not use the M^2

method, but instead directly choose the probability distribution for the point pairs ($|r| > 4$):

$$P_{24\mathrm{IL}}(r) \quad \propto \quad \frac{1}{|r|^4} e^{-0.01|r|}. \tag{4.16}$$

For the conserved method, the propagators are computed with approximate inversions carried out to a precision of 10^{-4}. (No correction term has been added.) The number of propagators needed per configuration (N_{prop}) is given by the sum of the number of point pairs times twice the number of propagators computed per point. For the conserved method, for each point we compute one point-source propagator and six sequential-source propagators, corresponding to the three external photon polarizations and two momentum directions.

For this implementation of the moment method we compute only the external momentum in the z direction, and external photon polarizations in x and y directions, so for each point we compute one point-source propagator and two sequential-source propagators for these two external photon polarizations. This is slightly different (and less effective) than the approach used for the moment method given in Table 4.7. The results are shown in Table 4.10 and a direct comparison between the $q^2 = 0$ results of the moment method (at two different muon source-sink separations) and the earlier $q^2 = (2\pi/L)^2$ results of Ref. [8] is shown in Fig. 4.5. As can be seen, a substantial improvement over the original calculation has been obtained. In addition, the good agreement between the earlier results and the new results using the conserved current method, both at $q^2 = (2\pi/L)^2$, provides a useful consistency check since these are two completely independent calculations.

4.5 QED light-by-light scattering results

In this section, we present results for QED light-by-light scattering in which the quark loop discussed in the previous sections is replaced by a muon loop. These calculations make use of the most effective of the numerical strategies discussed above: the use of exact photon propagators and the position-space moment method to determine F_2 evaluated at

Figure 4.5: A comparison of the results for $F_2(q^2)/(\alpha/\pi)^3$ obtained in the original lattice QCD cHLbL calculation [8] (diamonds) with those obtained on the same gauge field ensemble using the moment method presented here (circles). The points from the original subtraction method with $q^2 = (2\pi/24)^2 = (457\text{MeV})^2$ were obtained from 100 configurations and the evaluation of 81,000 point-source quark propagators for each value of the source-sink separation t_{sep}. In contrast, the much more statistically precise results from the moment method required a combined 26,568 quark propagator inversions for both values of t_{sep} and correspond to $q^2 = 0$. The moment method value for $t_{\text{sep}} = 32$ is listed in Table 4.10.

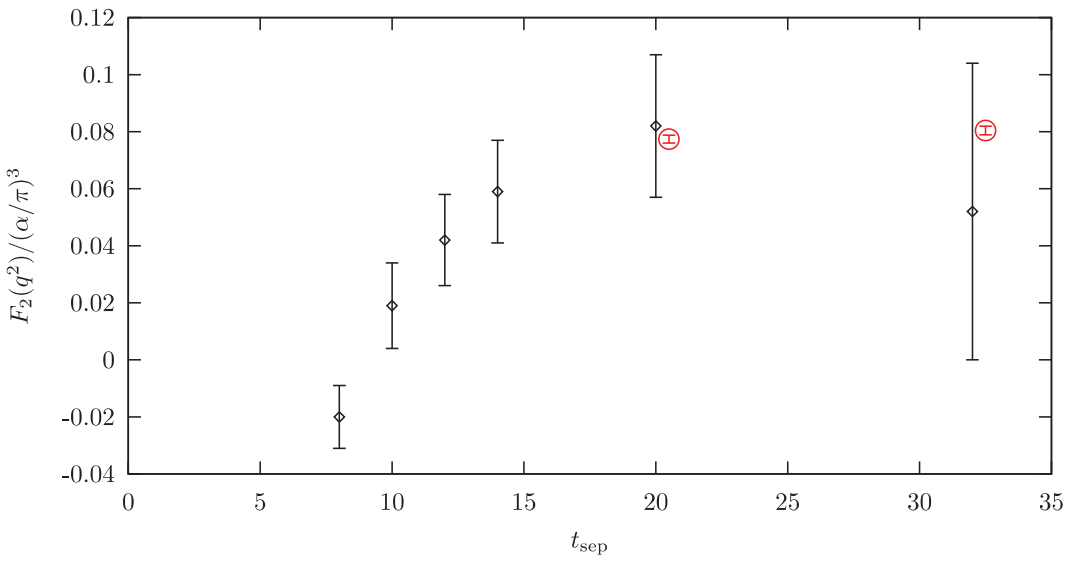

Table 4.10: Results for $F_2(q^2)$ from applying the conserved and moment methods to the the 24IL ensemble with $m_\mu a = 0.1$ using a muon source-sink separation $t_{\rm sep} = 32$. As before, $\sqrt{\rm Var} = {\rm Err}\sqrt{N_{\rm conf} N_{\rm prop}}$. We use the conserved current for the external photon and local currents for the internal photons for both methods. The conserved results are for $q^2 = (2\pi/L)^2$ while the moment methods gives a $q^2 = 0$ result.

Method	$F_2/(\alpha/\pi)^3$	$N_{\rm conf}$	$N_{\rm prop}$	$\sqrt{\rm Var}$
Conserved	0.0825(32)	12	$(118+128)\times 2\times 7$	0.65
Mom.	0.0804(15)	18	$(118+128)\times 2\times 3$	0.24

$q^2 = 0$. Since these calculations are less computationally costly than those for QCD, we can evaluate a number of volumes and lattice spacings (all specified with reference to the muon mass) and examine the continuum and infinite-volume limits. We can then compare our results, extrapolated to vanishing lattice spacing and infinite volume, with the known result calculated in standard QED perturbation theory [9, 10]. This QED calculation serves both as a demonstration of the capability of lattice methods to determine such light-by-light scattering amplitudes and as a first look at the size of the finite-volume and nonzero-lattice-spacing errors.

In Fig. 4.6 we show results for $F_2(0)$ computed for three different lattice spacings, *i.e.* three different values of the input muon mass in lattice units, but keeping the linear size of the system fixed in units of the muon mass. The data shown in Fig. 4.6 are also presented in Table 4.11. We use two extrapolation methods to obtain the continuum limit. The first, shown in the figure, uses a quadratic function of a^2 to extrapolate to $a^2 = 0$. The second makes a linear extrapolation to $a^2 = 0$ using only the two leftmost points for each of the three values of $m_\mu L$. The coefficients for the quadratic-in-a^2 fits shown in Fig. 4.6 as well as those for the linear-in-a^2 fits are given in tabular form in Tables. 4.12 and 4.13.

Figure 4.6: Plots of our results for the connected light-by-light scattering contribution in QED to $F_2(0)$, known to be $0.371 \times (\alpha/\pi)^3$ [9, 10], as a function of a^2 expressed in GeV by assigning $m_\mu = 106$ MeV. This is done for three choices of the physical lattice size $L = 11.9$ fm (diamonds), 8.9 fm (squares) and 5.9 fm (circles). The curves shown are quadratic functions of a^2 chosen to pass through the three points for each physical volume. The coefficients for each of these fits are listed in Table 4.13.

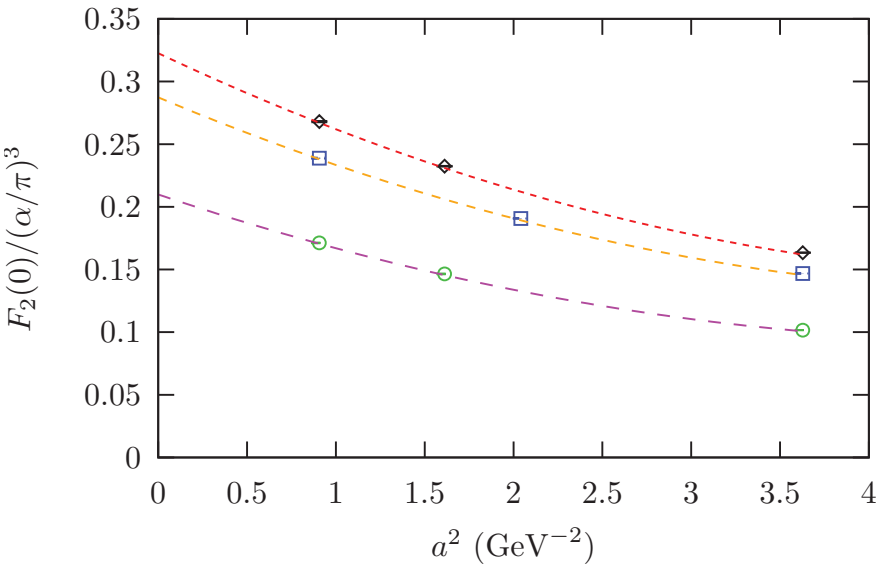

Table 4.11: A list of the input parameters, weights and numerical results for our QED calculations using the moment method. The right-most column shows the very accurate results from the short-distance, $|r| \leq r_{\max}$ region. These results are plotted in Fig. 4.6.

Vol	m_μ	$r_{\max}$	$p(x)$	N_{pair}	$F_2(0)/(\alpha/\pi)^3$	SD
$16^3 \times 64$	0.2	5	$\frac{\exp(-0.4\|x\|)}{\|x\|^4}$	1024	0.1016(1)	0.1000
$24^3 \times 96$	0.1333	6	$\frac{\exp(-0.25\|x\|)}{\|x\|^4}$	86	0.1465(3)	0.1428
$32^3 \times 128$	0.1	6	$\frac{\exp(-0.2\|x\|)}{\|x\|^4}$	194	0.1712(3)	0.1624
$24^3 \times 96$	0.2	6	$\frac{\exp(-0.4\|x\|)}{\|x\|^4}$	80	0.1468(1)	0.1451
$32^3 \times 128$	0.15	6	$\frac{\exp(-0.3\|x\|)}{\|x\|^4}$	50	0.1907(2)	0.1863
$48^3 \times 192$	0.1	6	$\frac{\exp(-0.2\|x\|)}{\|x\|^4}$	152	0.2388(5)	0.2243
$32^3 \times 128$	0.2	5	$\frac{\exp(-0.4\|x\|)}{\|x\|^4}$	276	0.1634(2)	0.1613
$48^3 \times 192$	0.1333	6	$\frac{\exp(-0.25\|x\|)}{\|x\|^4}$	189	0.2324(3)	0.2291
$64^3 \times 128$	0.1	6	$\frac{\exp(-0.2\|x\|)}{\|x\|^4}$	184	0.2680(5)	0.2592

Table 4.12: Functions quadratic in a^2 which fit the data shown in Fig. 4.6. The results from these fits at $a^2 = 0$ are plotted in Fig. 4.7.

L/fm	$F_2(0)/(\alpha/\pi)^3$
5.9	$0.2099(12) - 0.0478(13)(a\ \text{GeV})^2 + 0.0049(3)(a\ \text{GeV})^4$
8.9	$0.2873(13) - 0.0595(11)(a\ \text{GeV})^2 + 0.0056(2)(a\ \text{GeV})^4$
11.9	$0.3226(17) - 0.0669(17)(a\ \text{GeV})^2 + 0.0062(4)(a\ \text{GeV})^4$

Table 4.13: Functions linear in a^2 which can be used to extrapolate the data shown in Fig. 4.6 to $a^2 = 0$. The results from these fits at $a^2 = 0$ are plotted in Fig. 4.7.

L/fm	$F_2(0)/(\alpha/\pi)^3$
5.9	$0.2030(8) - 0.0357(6)(a\ \mathrm{GeV})^2$
8.9	$0.2773(9) - 0.0432(5)(a\ \mathrm{GeV})^2$
11.9	$0.3138(12) - 0.0515(9)(a\ \mathrm{GeV})^2$

In Fig. 4.7, we plot the $a^2 = 0$ values that result from the quadratic fit to the a^2 dependence given in Table 4.12 as a function of $1/(m_\mu L)^2$ along with the original perturbative result for these QED terms. There is clearly good agreement between an extrapolation linear in $1/(m_\mu L)^2$ using the two leftmost points and the known perturbative result. These fitting results, shown as functions of $m_\mu L$, are summarized in the following equations:

$$[F_2(0)]_{\mathrm{quad}}/(\alpha/\pi)^3 = 0.3679(42) - 1.86(11)/(m_\mu L)^2, \tag{4.17}$$

$$[F_2(0)]_{\mathrm{lin}}/(\alpha/\pi)^3 = 0.3608(30) - 1.92(8)/(m_\mu L)^2, \tag{4.18}$$

$$[F_2(0)]_{\mathrm{PT}}/(\alpha/\pi)^3 = 0.3710052921, \tag{4.19}$$

where the errors shown in Eqs. (4.17) and (4.18) are statistical only and the perturbative result is given in Eq. (4.19). We find very satisfactory agreement between the results from standard perturbation theory and the lattice results extrapolated to the continuum and infinite-volume limits.

Figure 4.7: Results for $F_2(0)$ from QED-connected light-by-light scattering. These results have been extrapolated to the $a^2 \to 0$ limit using two methods. The upper points use the quadratic fit to all three lattice spacings shown in Fig. 4.6, while the lower point uses a linear fit to the two leftmost points in that figure. Here we extrapolate to infinite volume using the linear fits shown to the two, leftmost of the three points in each case.

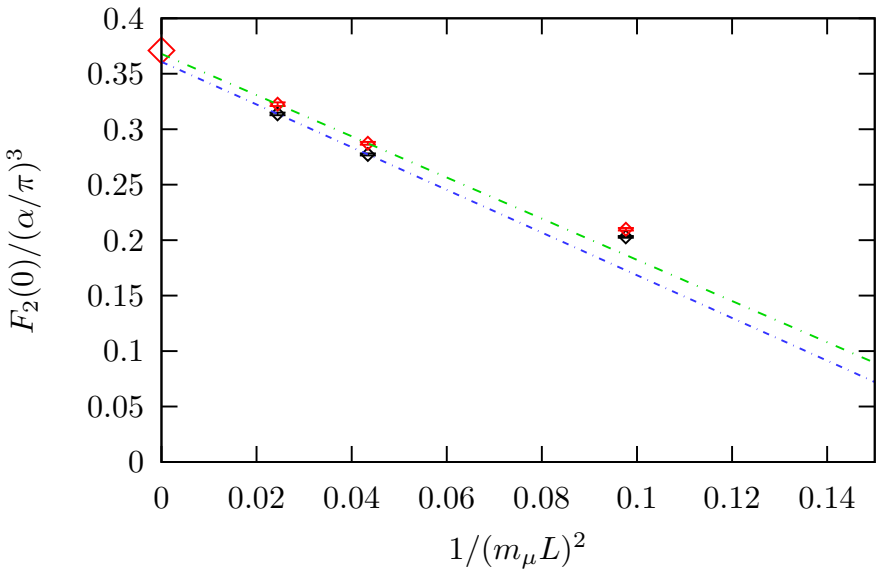

Chapter 5

Systematic Effects

So far, we have computed the cHLbL diagram at physical pion mass. The lattice size is $48^3 \times 96$, and corresponding physical volume is $(5.5 \text{ fm})^3$. In order to obtain the physical HLbL contribution to $g_\mu - 2$, there are three major systematic effects need to be addressed. First, the quark-disconnected diagrams need to be included. Second, we need to obtain the continuum limit. Third, we need to find the infinite volume limit of the current results. The continuum limit extrapolataion step, while very costly, should be straight forward. We can recompute the HLbL diagram with the same method, but using the 64I ensemble, an ensemble with lattice volume being $64^3 \times 128$ [5]. The parameters for 64I ensemble were adjusted so that it has roughly same properties as the 48I ensemble except a smaller lattice spacing. Just like the QED light-by-light calculation performed in Section 4.5, knowing that the finite lattice spacing effects are on the order of $\mathcal{O}(a^2)$, continuum extrapolataion can be performed with these two results. In the following two sections of this chapter, we discuss the other two kinds of systematic effects.

5.1 Quark-disconnected diagrams

There are many different quark-disconnected diagrams for HLbL. They are listed in Figure 5.1, 5.2, and 5.3. There are other possible permutations of the connections between the three internal photons and the muon line that are not shown. The quark loops are all connected by gluons which also are not drawn. The diagrams are categorized by their behaviour in the SU(3) limit. Since $e_u + e_d + e_s = 0$, any diagram with a loop connected to only one photon vanishes in SU(3) limit. Also, because the strange quark only carries 1/3 of the electron charge, diagrams that are suppressed by the difference between the strange and light quark masses are suppressed by their charge factors too.

We can evaluate the leading order diagram, Figure 5.1, using the same moment method that we use to compute the cHLbL diagram. The points x and z can be sampled, and used as sources for photon and quark propagators. The reference point for the moment method can be chosen to be z. This diagram without gluon lines connecting the two quark loops is not 1-particle irreducible, thus one may need to perform proper "vacuum" subtraction in order to only compute the vertex function [50]. However, when taking the moment with z as the reference point, the expectation value for the quark loop on the left side with an external photon is zero, thus no "vacuum" subtraction is needed for correctness. The other quark loop on the right with two internal photon, where we do not take the moment, has a non-zero expectation value. This none zero expectation value will not affect the final result because it will be multiplied by the expectation value of the left quark loop, which is zero. However, subtracting its expectation value from the right quark loop, one can reduce the statistical noise. Thus this subtraction should still be performed, but for variance-reduction reasons only.

Disconnected diagrams are usually much noisier than the connected diagrams. In the context of the HLbL calculation, the connected diagram has the advantage that both the signal and the noise decrease when the sampled points are separated by a large distance. As

Figure 5.1: Leading order diagram, survives in SU(3) limit.

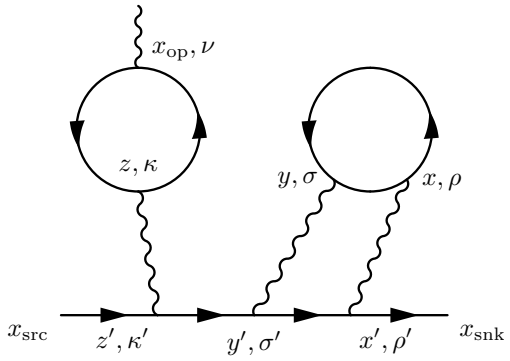

Figure 5.2: Next to leading order diagrams. $\mathcal{O}(m_s - m_l)$, vanishes in SU(3) limit.

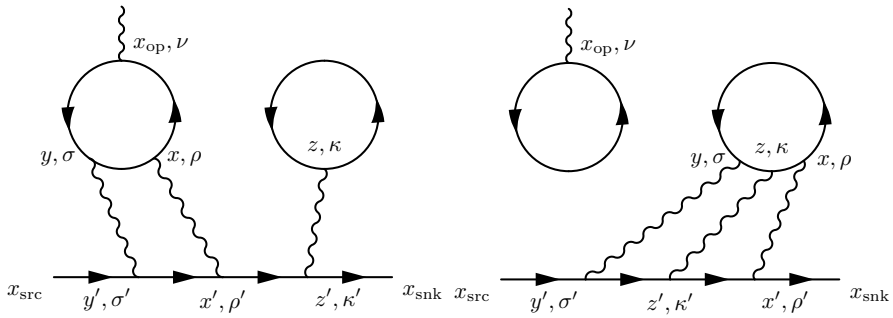

a result, not much effort is needed in order to control the error from the long distance region. For disconnected diagrams, the signal has to come from a subtle gluon interaction between the two quark loops, which only emerges after gauge averaging. As a result, although the signal is still exponentially suppressed when $|r| = |x - z|$ becomes large, the noise remains constant for arbitrary $|r|$. Since the formula involves summation over r, one can expect that a lot of noise will come from the large $|r|$ region, and this noise will become larger if we increase the volume. However, in terms of evaluating the diagram on the lattice, the independence of these two loops also provide some benefit. The contraction at y position does not depend on the position of z, allowing the M^2 trick to be applied without recomputing the muon part.

Figure 5.3: Even higher order diagrams.

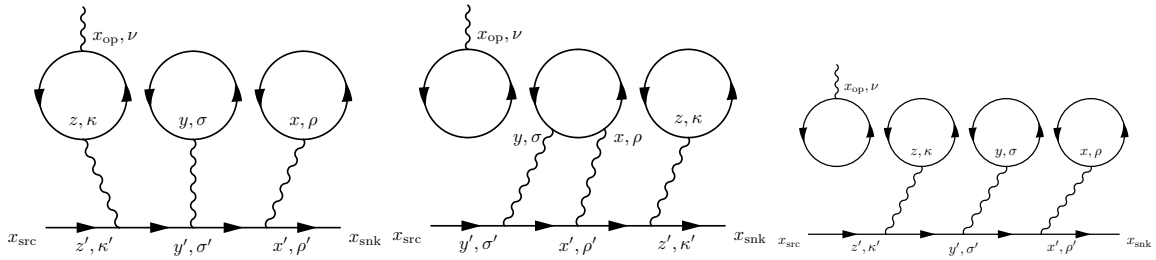

So, we obtain order M^2 combinations of samples with no additional cost, where M is the number of point source quark propagators computed for each configuration. This calculation of the leading-order diagram is now underway.

5.2 Infinite volume limit

Normally, the finite volume effects in lattice QCD calculations are exponentially suppressed as $e^{-m_\pi L}$ where L is the linear size of the lattice volume times and m_π, the energy of lowest mass particle of QCD. For example, the points x, y, z, which appear in Eq. (3.6), are directly connected by the quark loop. The finite volume effects introduced when these points are restricted to lie in a finite size lattice are exponentially suppressed. However, in the light-by-light calculation, there are also QED finite volume effects. The QED finite volume effects enter only through Eq. (3.7), which includes everything except the quark loop. We repeat

the equation below:

$$\begin{aligned}\mathcal{G}_{\rho\sigma\kappa}(x,y,z,x_{\rm snk},x_{\rm src}) \;=\; & \\ & \sum_{x',y',z'} G_{\rho\rho'}(x,x')G_{\sigma\sigma'}(y,y')G_{\kappa\kappa'}(z,z') \\ & \quad \cdot\Big[S_\mu\left(x_{\rm snk},x'\right)\gamma_{\rho'}S_\mu(x',z')\gamma_{\kappa'}S_\mu(z',y')\gamma_{\sigma'}S_\mu\left(y',x_{\rm src}\right) \\ & \qquad + S_\mu\left(x_{\rm snk},z'\right)\gamma_{\kappa'}S_\mu(z',x')\gamma_{\rho'}S_\mu(x',y')\gamma_{\sigma'}S_\mu\left(y',x_{\rm src}\right) \\ & \qquad + \text{four other permutations}\Big]. \end{aligned} \tag{5.1}$$

The summation variables x', y', z' in above equation can move freely along the muon line, and are only connected to the quark loop by massless photons. Thus, Eq. (5.1), when evaluated within a finite lattice with a finite muon source sink separation $x_{\rm snk} - x_{\rm src}$, will introduce finite volume errors suppressed only by powers of L. Another leading source of the finite volume errors in Eq. (5.1) comes from the photon propagators evaluated in a finite size lattice with periodic boundary conditions and its spatial zero modes are all dropped as described in Section 4.1. Overall, the finite volume effects in the HLbL calculation are on the order of $\mathcal{O}(1/L^2)$ as demonstrated by Figure 4.7 in the QED light-by-light calculation of Section 4.5.

Figure 5.4: Illustration of a QCD box inside QED box.

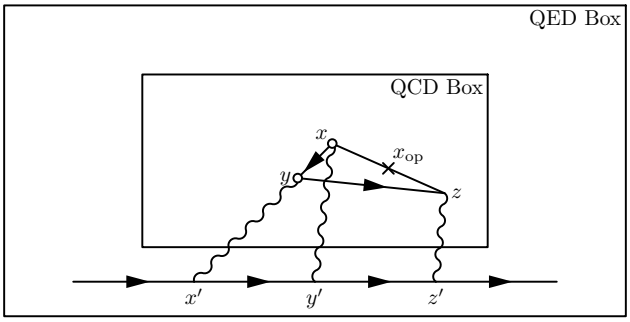

While Eq. (5.1) introduces $\mathcal{O}(1/L^2)$ finite volume effects, these effects do not involve

the quark propagator and do not depend on the QCD configurations. So, we can evaluate Eq. (5.1) using a volume larger than the volume of the QCD configuration. We refer to the former as the QED box and the latter as the QCD box, as in Figure 5.4. In fact, we can compute the light-by-light process for a few different QED boxes and extrapolate to the infinite volume result, reusing the same quark amplitudes. In this way, we can reduce the major part of the finite volume effects without generating larger QCD configurations or computing the quark propagator for a larger lattice. Also, since the hadronic part is the same for different QED box sizes, we expect there will exist strong correlations between these results, which would benefit the extrapolation. In principle, one could evaluate the muon and photon propagators using infinite volume formulae and perform the coordinate-space QED summation in infinite volume directly, thus completely eliminating this $\mathcal{O}(1/L^2)$ finite volume effect. In fact, this is exactly the strategy for the HVP calculation, where the usual approach [23] can be viewed as substituting the finite-volume result for $\Pi(q^2)$ into one- or two-loop QED calculations performed in infinite volume. At this point, one can see that computing the QED part of the diagram in a larger, possibly infinite, QED box is a quite general idea, and could be applied in many (but not necessarily all) other lattice QCD calculations involving QED. In some cases, such as the leading order QED correction to HVP diagram, all one needs is to evaluate the photon propagator in infinite volume.

We test the strategy of making the QED box larger than the QCD box by a calculation in 16^3 and 24^3 lattice volumes [44, 45] but with the same lattice spacing and pion mass. All computations are performed on 14 configurations separated by 200 MD time units and the results are shown in Table 5.1.

Table 5.1: Finite volume effects studies. $a^{-1} = 1.747$GeV, $m_\pi = 423$MeV, $m_\mu = 332$MeV.

Ensemble	QCD Size	QED Size	$t_{\rm snk} - t_{\rm src}$	$\frac{F_2(q^2=0)}{(\alpha/\pi)^3}$
16I [44]	$16^3 \times 32$	$16^3 \times 32$	16	0.1158(8)
24I [45]	$24^3 \times 64$	$24^3 \times 64$	32	0.2144(27)
16I-24 [44]	$16^3 \times 32$	$24^3 \times 64$	32	0.1674(22)

We can see that by using only a larger QED lattice, the major part of the finite-volume effects has been removed. However the disagreement between the results shown in the 2nd and 3rd lines of Table 5.1 implies that a $16^3 \times 32$ lattice with a spatial extent of 1.8 fm is not large enough to entirely suppress the QCD finite volume effect even for a heavier-than-physical pion mass of 420 MeV. To diagnose this disagreement, we plot the histograms for the contribution to F_2 for different separations of $|r| = |x - y|$ in the left plot of Figure 5.5. Note that the point z is summed over with the factor $\mathfrak{Z}(x, y, z)$ defined in Eq. 3.30. This choice of $\mathfrak{Z}$ restricts the summation region for z to exclude the part that is close to x and y, but includes the region close to the lattice boundary. As a result each bin of the histogram in the left panel of Figure 5.5 is affected by the QCD finite volume effects. To avoid this, we also examine the opposite choice, which provides more relevant information about the QCD finite-volume effects, using the z-distribution:

$$\mathfrak{Z}'(x,y,z) \;=\; \begin{cases} 3 & \text{if } |x-y| > |x-z| \text{ and } |x-y| > |y-z| \\ 3/2 & \text{if } |x-y| = |x-z| > |y-z| \text{ or } |x-y| = |y-z| > |x-z| \\ 1 & \text{if } |x-y| = |x-z| = |y-z| \\ 0 & \text{otherwise} \end{cases} \tag{5.2}$$

With this choice, in the small r region, the distances between x, y, z are all short, so the QCD finite volume effects should be small when $r = |x-y|$ is small. The right plot in Figure 5.5 suggests that it is indeed the case. In the small r region, where we control the QCD

finite volume effects, the result from the 16I QCD/24 QED calculation agrees very well with the 24I result. However, as $|r|$ becomes larger, the quark loop evaluated in 16I is affected by the boundary and begins to deviate from the 24I results. Because we use periodic boundary conditions for the quark propagators, the maximum spatial separation between source and sink in any direction is 8 for quark propagators on the 16I lattice and we see significant deviation between the 16I QCD/24 QED and 24I results when r becomes as large as 6.

Figure 5.5: Histograms of the contribution to F_2 from different separations $|r| = |x-y|$. The sum of all these points gives the final result for F_2. The vertical lines at $|r| = 5$ in the plots indicate the value of $r_{\max}$. The left plot is evaluated with $\mathfrak{Z}$, so the small r region includes most of the contribution. The right plot is evaluated with the z-distribution $\mathfrak{Z}'$ in place of $\mathfrak{Z}$, so the QCD finite volume effects are better controlled in the small r region.

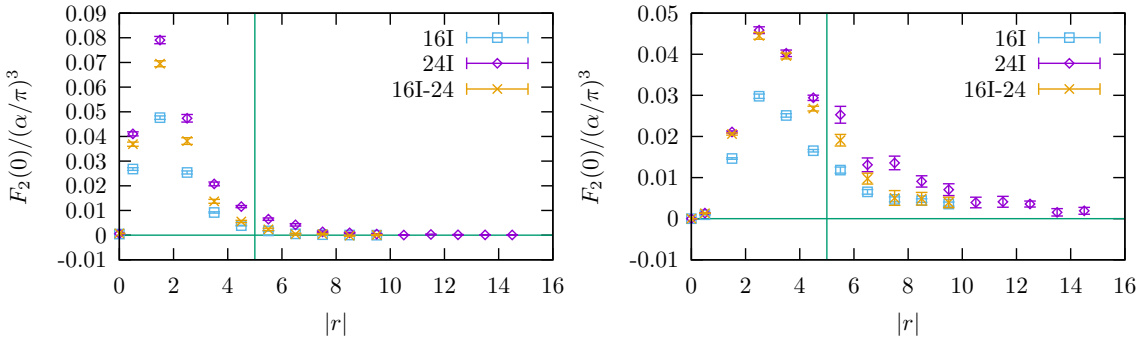

The agreement of the 16I QCD/24 QED calculation and the 24I calculation in the small r region proves the success of the QCD box inside QED box method. The size of the contribution in the large r region provides an indication for the QCD finite volume effects. We plot the histograms in Figure 5.6 with $\mathfrak{Z}'$ along with the results obtained previously, shown in Figure 4.4 for the physical-pion-mass 48I ensemble. As can be seen from the right plot in Figure 5.6, the signal has become very small well before $r = 24$, the midpoint of the 48^3 lattice volume. Thus, the finite QCD volume is likely to be sufficiently large that

evaluating the QED part in a larger volume should correct most of the finite volume errors.

Figure 5.6: Histograms of the contribution to F_2 from different separations $|r| = |x - y|$. The sum of all these points gives the final result for F_2. The vertical lines at $|r| = 5$ indicate the value of $r_{\max}$. The left plot is evaluated with the z-distribution $\mathfrak{Z}$, so the small r region includes most of the contribution. The right plot is evaluated with $\mathfrak{Z}'$ in place of $\mathfrak{Z}$, so the QCD finite volume effects are better controlled in the small r region. We use 34 configurations each separated by 40 MD time units to make the plot on the right.

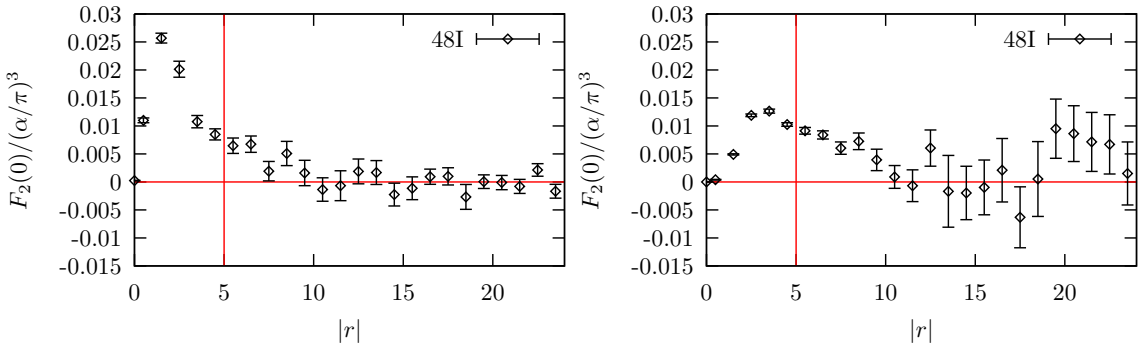

Chapter 6

Conclusion and Outlook

In this thesis we have extended the lattice field theory methods introduced in Ref. [8], increasing the computational efficiency by more than 2 orders of magnitude and allowing the calculation of the q^2-dependent form factor $F_2(q^2)$ directly at $q^2 = 0$ instead of at $(2\pi/L)^2$, the smallest, nonzero momentum accessible in finite volume. To demonstrate the correctness of our methods, we have studied the light-by-light scattering contribution within QED, arising when the internal loop is a muon, working at three values for the lattice spacing and three volumes. By extrapolating to vanishing lattice spacing and infinite volume we obtain a result which agrees with the analytic result within 2%, an accuracy expected from a combination of statistical and extrapolation uncertainties.

The most successful approach uses exact, analytic formulas for the three photon propagators that appear in the HLbL amplitude and the standard methods of lattice QCD. In contrast with normal perturbative methods, much of the calculation is performed in position space and stochastic methods are only introduced to sample position-space sums, reducing the computational cost so that it grows proportionally to the space-time volume instead of its cube. Because of the structure of the amplitude being computed, we can identify a specific space-time position within the hadronic part of the amplitude and use that location as the origin to obtain the anomalous magnetic moment from what is essentially a classical

spatial moment of the quantum distribution of current.

These new methods are used to obtain a result for the cHLbL contribution to $g_\mu - 2$ from a relatively coarse $48^3 \times 96$ ensemble with $1/a = 1.73$ GeV, spatial extent $L = 5.5$ fm and pion mass $m_\pi = 139$ MeV:

$$\frac{(g_\mu - 2)_{\mathrm{cHLbL}}}{2} = (0.933 \pm 0.0073)(\alpha/\pi)^3 = (116.9 \pm 9.1) \times 10^{-11}, \tag{6.1}$$

which can be compared to the conventional model-dependent result for the complete HLbL contribution to $g_\mu - 2$ of $(105 \pm 26) \times 10^{-11}$ and the difference between the current experimental result and the standard model prediction (excluding the HLbL component) of $(354 \pm 86) \times 10^{-11}$. Equation (6.1) shows only the statistical error. There are significant systematic errors associated with the nonzero lattice spacing and the finite volume that have been used in this calculation. These systematic errors are at present insufficiently well understood to be reliably estimated. A particularly important systematic error comes from the omission of the quark-disconnected contributions, which play an important role in the phenomenological estimates. Thus, the comparison of the result in Eq. (6.1) with experiment serves only to give a context for the size of the present statistical errors.

In Chapter 4 we have presented a series of numerical tests of many of the different methods that were explored while developing the methods that were finally used to obtain the result in Eq. (6.1). We hope that some of these may be useful in the future for the efficient calculation of other quantities that involve a combination of QED and QCD, a relatively new area where there are many new directions to explore.

The cHLbL calculation at physical pion mass presented here has been performed on current leadership-class computers. A follow-on calculation with a smaller lattice spacing and a corresponding $64^3 \times 128$ volume is planed, allowing a continuum limit to be evaluated. Controlling the effects of finite volume and including the contributions of disconnected diagrams are more difficult, but they are being actively pursued. For now, we may guess the size of discretization and finite volume effects based on our QED light-by-light calcuation

described in Section 4.5. We estimate the above result may have 20% discretization errors and significant finite volume errors. As a result, the infinite volume, continuum value for the connected light-by-light contribution could be twice as large as the current value in Eq. (6.1). However, the disconnected light-by-light diagrams may contribute negatively and cancel part of the above enhancement.

Bibliography

[1] Michel Davier, Andreas Hoecker, Bogdan Malaescu, and Zhiqing Zhang. Reevaluation of the Hadronic Contributions to the Muon g-2 and to alpha(MZ). *Eur.Phys.J.*, C71:1515, 2011.

[2] Kaoru Hagiwara, Ruofan Liao, Alan D. Martin, Daisuke Nomura, and Thomas Teubner. $(g-2)_\mu$ and alpha(M_Z^2) re-evaluated using new precise data. *J.Phys.*, G38:085003, 2011.

[3] Y. Aoki et al. Continuum Limit Physics from 2+1 Flavor Domain Wall QCD. *Phys.Rev.*, D83:074508, 2011.

[4] R. Arthur et al. Domain Wall QCD with Near-Physical Pions. *Phys.Rev.*, D87:094514, 2013.

[5] T. Blum et al. Domain wall QCD with physical quark masses. *Phys. Rev.*, D93(7):074505, 2016.

[6] Luchang Jin. Lattice Calculation of the Hadronic Light by Light Contributions to the Muon Anomalous Magnetic Moment. *PoS*, LATTICE2014:130, 2014.

[7] Joaquim Prades, Eduardo de Rafael, and Arkady Vainshtein. Hadronic Light-by-Light Scattering Contribution to the Muon Anomalous Magnetic Moment. 2009.

[8] Thomas Blum, Saumitra Chowdhury, Masashi Hayakawa, and Taku Izubuchi. Hadronic light-by-light scattering contribution to the muon anomalous magnetic moment from lattice QCD. *Phys.Rev.Lett.*, 114(1):012001, 2015.

[9] S. Laporta and E. Remiddi. The Analytic value of the light-light vertex graph contributions to the electron (g-2) in QED. *Phys. Lett.*, B265:182–184, 1991.

[10] Fred Jegerlehner and Andreas Nyffeler. The Muon g-2. *Phys. Rept.*, 477:1–110, 2009.

[11] D. Hanneke, S. Fogwell, and G. Gabrielse. New Measurement of the Electron Magnetic Moment and the Fine Structure Constant. *Phys. Rev. Lett.*, 100:120801, 2008.

[12] D. Hanneke, S. Fogwell Hoogerheide, and G. Gabrielse. Cavity Control of a Single-Electron Quantum Cyclotron: Measuring the Electron Magnetic Moment. *Phys. Rev.*, A83:052122, 2011.

[13] Tatsumi Aoyama, Masashi Hayakawa, Toichiro Kinoshita, and Makiko Nio. Tenth-Order QED Contribution to the Electron g-2 and an Improved Value of the Fine Structure Constant. *Phys. Rev. Lett.*, 109:111807, 2012.

[14] Tatsumi Aoyama, M. Hayakawa, Toichiro Kinoshita, and Makiko Nio. Tenth-Order Electron Anomalous Magnetic Moment — Contribution of Diagrams without Closed Lepton Loops. *Phys. Rev.*, D91(3):033006, 2015.

[15] Peter J. Mohr, Barry N. Taylor, and David B. Newell. CODATA Recommended Values of the Fundamental Physical Constants: 2010. *Rev. Mod. Phys.*, 84:1527–1605, 2012.

[16] Rym Bouchendira, Pierre Clade, Saida Guellati-Khelifa, Francois Nez, and Francois Biraben. New determination of the fine structure constant and test of the quantum electrodynamics. *Phys. Rev. Lett.*, 106:080801, 2011.

[17] K. A. Olive et al. Review of Particle Physics. *Chin. Phys.*, C38:090001, 2014.

[18] James P. Miller, Eduardo de Rafael, and B. Lee Roberts. Muon (g-2): Experiment and theory. *Rept.Prog.Phys.*, 70:795, 2007.

[19] G.W. Bennett et al. Final Report of the Muon E821 Anomalous Magnetic Moment Measurement at BNL. *Phys.Rev.*, D73:072003, 2006.

[20] Tatsumi Aoyama, Masashi Hayakawa, Toichiro Kinoshita, and Makiko Nio. Complete Tenth-Order QED Contribution to the Muon g-2. *Phys.Rev.Lett.*, 109:111808, 2012.

[21] Alexander Kurz, Tao Liu, Peter Marquard, and Matthias Steinhauser. Hadronic contribution to the muon anomalous magnetic moment to next-to-next-to-leading order. *Phys.Lett.*, B734:144–147, 2014.

[22] C. Gnendiger, D. Stckinger, and H. Stckinger-Kim. The electroweak contributions to $(g-2)_\mu$ after the Higgs boson mass measurement. *Phys.Rev.*, D88:053005, 2013.

[23] T. Blum. Lattice calculation of the lowest order hadronic contribution to the muon anomalous magnetic moment. *Phys.Rev.Lett.*, 91:052001, 2003.

[24] Thomas Blum, Achim Denig, Ivan Logashenko, Eduardo de Rafael, B. Lee Roberts, et al. The Muon (g-2) Theory Value: Present and Future. 2013.

[25] Maurice Benayoun, Johan Bijnens, Tom Blum, Irenel Caprini, Gilberto Colangelo, et al. Hadronic contributions to the muon anomalous magnetic moment Workshop. $(g-2)_\mu$: Quo vadis? Workshop. Mini proceedings. 2014.

[26] T. Blum, P. A. Boyle, T. Izubuchi, L. Jin, A. Jttner, C. Lehner, K. Maltman, M. Marinkovic, A. Portelli, and M. Spraggs. Calculation of the hadronic vacuum polarization disconnected contribution to the muon anomalous magnetic moment. 2015.

[27] Justin Foley, K. Jimmy Juge, Alan O'Cais, Mike Peardon, Sinead M. Ryan, and Jon-Ivar Skullerud. Practical all-to-all propagators for lattice QCD. *Comput. Phys. Commun.*, 172:145–162, 2005.

[28] Thomas Blum, Taku Izubuchi, and Eigo Shintani. New class of variance-reduction techniques using lattice symmetries. *Phys. Rev.*, D88(9):094503, 2013.

[29] Eigo Shintani, Rudy Arthur, Thomas Blum, Taku Izubuchi, Chulwoo Jung, and Christoph Lehner. Covariant approximation averaging. *Phys. Rev.*, D91(11):114511, 2015.

[30] Gilberto Colangelo, Martin Hoferichter, Massimiliano Procura, and Peter Stoffer. Dispersive approach to hadronic light-by-light scattering. *JHEP*, 1409:091, 2014.

[31] Gilberto Colangelo, Martin Hoferichter, Bastian Kubis, Massimiliano Procura, and Peter Stoffer. Towards a data-driven analysis of hadronic light-by-light scattering. *Phys.Lett.*, B738:6–12, 2014.

[32] Vladyslav Pauk and Marc Vanderhaeghen. Two-loop massive scalar three-point function in a dispersive approach. 2014.

[33] Vladyslav Pauk and Marc Vanderhaeghen. Anomalous magnetic moment of the muon in a dispersive approach. *Phys.Rev.*, D90(11):113012, 2014.

[34] Gilberto Colangelo, Martin Hoferichter, Massimiliano Procura, and Peter Stoffer. Dispersion relation for hadronic light-by-light scattering: theoretical foundations. *JHEP*, 09:074, 2015.

[35] David B. Kaplan. A Method for simulating chiral fermions on the lattice. *Phys. Lett.*, B288:342–347, 1992.

[36] Vadim Furman and Yigal Shamir. Axial symmetries in lattice QCD with Kaplan fermions. *Nucl. Phys.*, B439:54–78, 1995.

[37] Martin Luscher. Abelian chiral gauge theories on the lattice with exact gauge invariance. *Nucl. Phys.*, B549:295–334, 1999.

[38] Maarten Golterman and Yigal Shamir. SU(N) chiral gauge theories on the lattice. *Phys. Rev.*, D70:094506, 2004.

[39] Dorota M. Grabowska and David B. Kaplan. A Nonperturbative Regulator for Chiral Gauge Theories. 2015.

[40] H. J. Rothe. Lattice gauge theories: An Introduction. *World Sci. Lect. Notes Phys.*, 43:1–381, 1992. [World Sci. Lect. Notes Phys.82,1(2012)].

[41] Richard C. Brower, Harmut Neff, and Kostas Orginos. The Móbius Domain Wall Fermion Algorithm. 2012.

[42] Masashi Hayakawa, Thomas Blum, Taku Izubuchi, and Norikazu Yamada. Hadronic light-by-light scattering contribution to the muon g-2 from lattice QCD: Methodology. *PoS*, LAT2005:353, 2006.

[43] J. D. Jackson. *Classical Electrodynamics*. Wiley , New York, NY, 1999. see Section 5.6.

[44] C. Allton et al. 2+1 flavor domain wall QCD on a (2 fm)*83 lattice: Light meson spectroscopy with L(s) = 16. *Phys.Rev.*, D76:014504, 2007.

[45] C. Allton et al. Physical Results from 2+1 Flavor Domain Wall QCD and SU(2) Chiral Perturbation Theory. *Phys.Rev.*, D78:114509, 2008.

[46] T. Blum et al. Quenched lattice qcd with domain wall fermions and the chiral limit. *Phys. Rev.*, D69:074502, 2004.

[47] Sinya Aoki, Taku Izubuchi, Yoshinobu Kuramashi, and Yusuke Taniguchi. Perturbative renormalization factors in domain wall QCD with improved gauge actions. *Phys. Rev.*, D67:094502, 2003.

[48] Masashi Hayakawa and Shunpei Uno. QED in finite volume and finite size scaling effect on electromagnetic properties of hadrons. *Prog. Theor. Phys.*, 120:413–441, 2008.

[49] Hantao Yin and Robert D. Mawhinney. Improving DWF Simulations: the Force Gradient Integrator and the Móbius Accelerated DWF Solver. *PoS*, LATTICE2011:051, 2011.

[50] M. Hayakawa, T. Blum, N. H. Christ, T. Izubuchi, L. C. Jin, and C. Lehner. On calculating disconnected-type hadronic light-by-light scattering diagrams from lattice QCD. In *Proceedings, 33rd International Symposium on Lattice Field Theory (Lattice 2015)*, 2015.

[51] James D. Bjorken and Sidney D. Drell. Relativistic quantum fields. 1965.

[52] Jean Zinn-Justin. Quantum field theory and critical phenomena. *Int.Ser.Monogr.Phys.*, 113:1–1054, 2002.

Appendix A

Avoiding lattice artifacts in the HLbL amplitude

In standard continuum perturbation theory the Feynman graphs which enter the HLbL contribution to $g_\mu - 2$ contain no divergences beyond the usual mass, wave function and coupling constant renormalizations that result from either the QED or QCD interactions. In fact, because of the limited topologies for the photon couplings which appear in these HLbL amplitudes, even these standard QED renormalizations are not required. However, when a lattice regulator is used, the choice of electromagnetic couplings may change this situation. Wilson's formulation of lattice gauge theory introduces couplings between the quarks and gluons which explicitly preserve the Yang-Mills gauge symmetry even at finite lattice spacing and guarantees that gauge-noninvariant counterterms will not be needed to ensure that the lattice theory has a continuum limit.

Following the same strategy, we can avoid the appearance of new, unwanted short-distance contributions in a HLbL lattice calculation by introducing quark-photon and muon-photon couplings which are invariant under QED gauge symmetry. This is quite manageable if a single photon is to be coupled to a muon or quark line: we can introduce the conserved

lattice current which contains fermion fields evaluated at both ends of the given lattice link associated with the current operator. However, if two or three photons are coupled to the same fermion line, then the nonlocality of the conserved current used to couple the first photon requires that additional two- and three-photon vertices be introduced if electromagnetic gauge invariance is to be preserved. The resulting calculation can still be performed but at the cost of considerable complexity.

In this appendix, we will demonstrate that new $O(1)$ lattice artifacts can be avoided in the case of the HLbL amplitude by the simple precaution of using the conserved lattice current when coupling the external photon to the quark loop. The other six electromagnetic couplings can be given by the standard local current, provided the six necessary Z_V renormalization factors are introduced. The use of the conserved current for the external photon is only needed for the connected graph. For the disconnected HLbL amplitudes the simpler local current can be used for all photon couplings.

The absence of new short-distance contributions when a local current is used for all internal photon couplings in a lattice-regulated calculation of HLbL can be seen by examining the HLbL amplitude in a Feynman perturbation theory expansion carried out to arbitrary order in the QCD coupling. A convenient approach organizes the QCD perturbation theory into skeleton graphs and analyzes each skeleton graph [51, 52]. Recall that a skeleton graph in this context will be a graph with three internal photon lines and arbitrary quark and gluon lines subject to the restriction that no self-energy or proper vertex subgraphs appear. Each vertex in such a skeleton graph represents a sum over all one-particle irreducible QCD vertex graphs. Likewise, each propagator in such a skeleton graph represents a sum over all QCD gluon or quark self-energy diagrams. In Fig. A.1 we show a sample HLbL graph and the corresponding skeleton graph.

Each such skeleton graph can be expanded into a sum of ordinary graphs by replacing each vertex and propagator with the corresponding sums over all vertex and propagator

Figure A.1: The left-hand graph shows a sample QCD+QED diagram contributing to the HLbL amplitude. The black dot in this diagram represents the current to which the external photon couples. The right-hand graph shows the skeleton graph to which this sample graph contributes. Here the shaded disk with the black dot on its circumference represents the full vertex function containing the current to which the external photon couples.

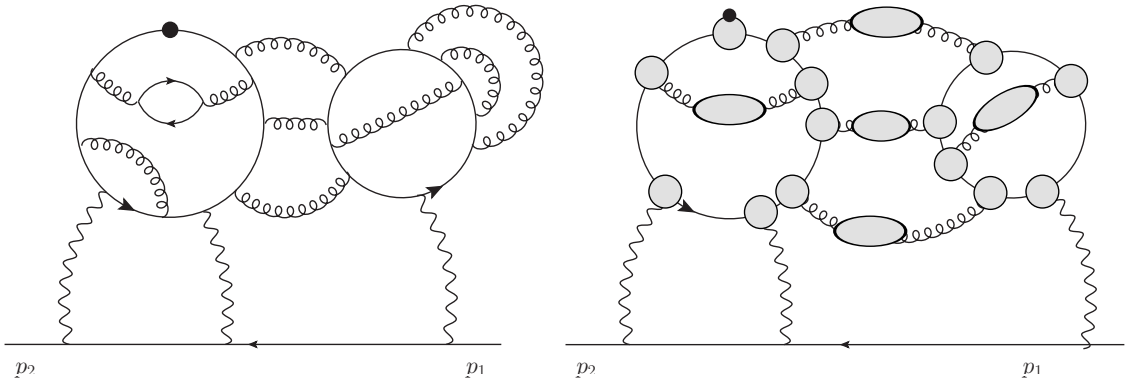

subgraphs. Likewise, a general graph can be identified with a skeleton graph if each vertex and self-energy subgraph appearing in that general graph is replaced with a simple vertex or propagator. It can be shown that this process yields a unique skeleton graph independent of the order in which this replacement is made, provided that the entire graph is not itself a self-energy graph, which it is not in the present HLbL case. In a standard skeleton graph expansion, the three internal photon propagators may themselves be part of a proper vertex or self-energy subgraph and would then not appear in the final skeleton graph. However, for the HLbL case where each internal photon line is coupled to the single muon line which passes through the diagram, the only vertex or self-energy subgraph which contains one or more internal photon lines is the entire graph.

We will now show that each of the six internal photon vertices in this skeleton expansion can be accurately implemented if the internal photon is coupled to Z_V multiplied by the local lattice current for each of the vertex subgraphs represented by that vertex in the skeleton graph expansion. This will be the case if the momentum carried by each of the three external

lines connected to that vertex is small compared to the regulator scale, which in our case is the inverse lattice spacing $1/a$. It is for such physical-scale momenta that Z_V times the local current and the conserved lattice current will agree. Thus, we need to show that all skeleton subgraphs which contain such a complete internal photon vertex have a negative degree of divergence. Such a convergent character for all graphs in which each internal photon vertex appears will guarantee that when the momentum entering that vertex is of order $1/a$, this will correspond to a momentum integration region which is suppressed by at least two inverse powers of $1/a$, which results in a small $O(a^2)$ error.

There are two types of skeleton graphs with a non-negative degree of divergence. The first is the entire HLbL graph itself, which as a vertex graph has zero degrees of divergence. However, for the case of the magnetic form factor F_2 being examined here, we are considering a term which is even under conjugation with γ^5. Such a chirality-changing amplitude will vanish unless an explicit factor of the muon mass is present and the presence of such a mass factor implies that the graph has a degree of divergence -1 or smaller, guaranteeing suppression of the momentum region when all internal lines carry large momenta.

The other type of subgraph, which is neither a vertex nor a self-energy subgraph, but which has a potentially non-negative degree of divergence, contains an internal quark loop coupled to four gluon or photon lines which are external lines of that subgraph. In a gauge-invariant regularization scheme in which these gluons and photons couple to conserved currents, the corresponding Ward identities will guarantee that each of these currents is transverse which requires that the entire amplitude contain two or more explicit factors of the momenta carried by these four external gluons or photons. The presence of these momentum factors reduces the zero degrees of divergence of such a graph with four external boson lines, resulting in a negative degree of divergence. Since each gluon couples to a conserved current which guarantees convergence of the subgraph, the only subgraphs at issue are those with four external photon lines.

Such subgraphs do appear in the HLbL amplitude and correspond to a quark loop with general internal gluon couplings, but the only external vertices possessed by that subgraph are those of the three internal photons and the external current. Thus, each such subgraph will have zero degrees of divergence unless we require that one of these four couplings involve an exactly conserved current. Thus, our choice that the photon external to the entire HLbL graph couples to a conserved current guarantees that this is the case. Under these circumstances an explicit external momentum factor must be present and the subgraph must have a negative degree of divergence. Note that this class of diagram which can be made convergent by the introduction of the conserved external current corresponds only to the connected cHLbL case studied in this thesis. Such a conserved current coupling is not required for any of the disconnected graphs.

In this discussion we have assumed that the three internal photons couple to the quark and muon lines through a local current. We have not been concerned about the short distance form of this local current since this will only affect the form of the coupling when large momentum flows through the vertex given by that current. For a nonconserved local current this will act only to change the normalization of the current, an effect which is corrected by the introduction of the factor of Z_V. We can also include more complex couplings for the internal photons without changing the final result. For example, if additional dimension-6, two-quark, three-photon couplings are introduced, the degree of divergence of these subgraphs will be increased and could become non-negative. Such a dimension-6 vertex would result in subgraphs with two quark and three photon external lines with degree of divergence increased from -2 to 0. However, the factor of a^2 that must accompany such a dimension-6 lattice operator would ensure that its effects would vanish as a^2 in the continuum limit.

Appendix B

Conventional interpretation of moment formula

Equation (3.27) derived in Sec. 3.4 provides a very effective way to obtain $g_\mu - 2$ from a first moment of the finite-volume cHLbL amplitude evaluated directly at zero momentum transfer. In this appendix we provide additional context for this equation by showing its relation to the conventional formula given in Eq. (3.28) for the magnetic moment resulting from a localized static current distribution. We begin by repeating Eq. (3.27):

$$\frac{F_2(0)}{2m_\mu}\overline{u}(\vec{0},s')\,\vec{\Sigma}\,u(\vec{0},s) \;=\; \frac{1}{2}\sum_{r,z,x_{\rm op}} \vec{x}_{\rm op}\times i\overline{u}(\vec{0},s')\,\vec{\mathcal{F}}^C\left(\frac{r}{2},-\frac{r}{2},z,x_{\rm op}\right)u(\vec{0},s). \qquad \text{(B.1)}$$

While this equation is suggestive of the conventional Eq. (3.28) for the magnetic moment there are three significant differences: (i) An internal coordinate in the Feynman amplitude on the right-hand side of Eq. (B.1), the variable $w = (x + y)/2$, is fixed at zero when it should be integrated over space-time in a perturbative evaluation of the matrix element of the current $\vec{J}(x_{\rm op})$ in Eq. (3.28); (ii) the time coordinate of the current, $(x_{\rm op})_0$ is integrated instead of being held fixed; and (iii) the factor of $1/V$ which is required if the initial and final muon states are to be properly normalized is missing. As we will see, these three differences between Eqs. (3.27) or (B.1) and Eq. (3.28) mutually compensate.

The first step in this demonstration exploits the symmetry of $\vec{\mathcal{F}}^C\left(\frac{r}{2}, -\frac{r}{2}, z, x_{\rm op}\right)$ under time translation to subtract $(x_{\rm op})_0$ from each of the four time arguments in Eq. (B.1). This step will result in the external current being evaluated at $t = 0$, an easily absorbed shift in the summation variable z_0 and the appearance of two independent summations over the time arguments of the points x and y, allowing us to write Eq. (B.1) as

$$\frac{F_2(0)}{2m_\mu}\overline{u}(\vec{0}, s')\,\vec{\Sigma}\,u(\vec{0}, s) \tag{B.2}$$
$$= \frac{1}{2}\sum_{\substack{\vec{r}, x_0, y_0 \\ z, \vec{x}_{\rm op}}} \vec{x}_{\rm op} \times i\overline{u}(\vec{0}, s')\,\vec{\mathcal{F}}^C\left((x_0, \frac{\vec{r}}{2}), (y_0, -\frac{\vec{r}}{2}), z, (0, \vec{x}_{\rm op})\right) u(\vec{0}, s),$$

where we have written the previous x and y vertices as the four-vectors $(x_0, \frac{\vec{r}}{2})$ and $(y_0, -\frac{\vec{r}}{2})$, respectively, and absorbed the $(x_{\rm op})_0$ shift into the summation variable z.

Next, we turn to the conventional formula, adapted to our quantum mechanical circumstances:

$$\langle\psi'|\psi\rangle(\vec{\mu})_{s',s} = \frac{1}{2}\sum_{\vec{x}_{\rm op}} \vec{x}_{\rm op} \times \left\{\sum_{\vec{p}'\vec{p}} \widetilde{\psi}'(\vec{p}')^* \Big\langle \mu(\vec{p}', s')\Big|\vec{J}(0, \vec{x}_{\rm op})\Big|\mu(\vec{p}, s)\Big\rangle \widetilde{\psi}(\vec{p})\right\}, \tag{B.3}$$

where $\widetilde{\psi}'(\vec{p}')$ and $\widetilde{\psi}(\vec{p})$ are momentum-space wave functions that describe initial and final muon states which are localized at the origin, which itself is chosen to be far from the walls of the large, finite volume in which the calculation is being performed. (The wave functions $\widetilde{\psi}'(\vec{p}')$ and $\widetilde{\psi}(\vec{p})$ are normalized to $1/V$ to compensate for the states $|\mu(\vec{p}', s')\rangle$ and $|\mu(\vec{p}, s)\rangle$ being un-normalized plane waves.) A non-relativistic form has been assumed for the expression on the left-hand side. Finally, we can recover Eq. (B.2) from Eq. (B.3) if we replace the matrix element between momentum eigenstates with the Feynman amplitude $i\overline{u}(\vec{p}', s')\vec{\mathcal{F}}^C(x, y, z, x_{\rm op})u(\vec{p}, s)$ that appears in Eq. (B.2):

$$\langle\psi'|\psi\rangle(\vec{\mu})_{s',s} = -\frac{e}{2}\sum_{\vec{x}_{\rm op}} \vec{x}_{\rm op} \times \left\{\sum_{\vec{p}'\vec{p}} \widetilde{\psi}'(\vec{p}')^* \sum_{\vec{w}} i\overline{u}(\vec{p}', s')\vec{\mathcal{F}}^C\Big(\vec{w}, (0, \vec{x}_{\rm op})\Big)u(\vec{p}, s)\widetilde{\psi}(\vec{p})\right\}, \tag{B.4}$$

where for clarity we display only the internal vector $\vec{w} = (\vec{x}+\vec{y})/2$ in addition to $x_{\rm op}$. We can use the translational covariance of $\mathcal{F}$ to extract the variable $\vec{w}$, rename the shifted variable

$\vec{x}_{\rm op} - \vec{w}$ to simply $\vec{x}_{\rm op}$ and invoke current conservation to drop the added $\vec{w}$ that will appear in the left-hand factor of $\vec{x}_{\rm op}$ when this renaming is done. We obtain:

$$\langle\psi'|\psi\rangle(\vec{\mu})_{s',s} \tag{B.5}$$
$$= -\frac{e}{2}\sum_{\vec{x}_{\rm op}} \vec{x}_{\rm op} \times \left\{ \sum_{\vec{p}'\vec{p}} \widetilde{\psi}'(\vec{p}')^* \sum_{\vec{w}} e^{i\vec{w}\cdot(\vec{p}-\vec{p}')} i\overline{u}(\vec{p}',s')\vec{\mathcal{F}}^C\Big(\vec{0},(0,\vec{x}_{\rm op})\Big)u(\vec{p},s)\widetilde{\psi}(\vec{p}) \right\}.$$

If we assume that $\vec{p}$ and $\vec{p}'$ are both small on the scale over which $\overline{u}(\vec{p}',s')\vec{\mathcal{F}}^C u(\vec{p},s)$ varies, this equation reduces to Eq. (B.2) since the factor

$$\sum_{\vec{p},\vec{p}',\vec{w}} \widetilde{\psi}'(\vec{p}')^* e^{i\vec{w}\cdot(\vec{p}-\vec{p}')}\widetilde{\psi}(\vec{p}) = \langle\psi'|\psi\rangle, \tag{B.6}$$

which can now be recognized on the right-hand side, cancels that on the left.

Appendix C

Conventions

We adopt the following gamma matrix convention:

$$\sigma_x = \begin{pmatrix} 0 & 1 \\ 1 & 0 \end{pmatrix} \quad \sigma_y = \begin{pmatrix} 0 & -i \\ i & 0 \end{pmatrix} \quad \sigma_z = \begin{pmatrix} 1 & 0 \\ 0 & -1 \end{pmatrix}. \tag{C.1}$$

$$\begin{aligned} \gamma_0 &= \begin{pmatrix} 0 & 1 \\ 1 & 0 \end{pmatrix}, \quad \gamma_1 = -i \begin{pmatrix} 0 & \sigma_x \\ -\sigma_x & 0 \end{pmatrix}, \quad \gamma_2 = -i \begin{pmatrix} 0 & \sigma_y \\ -\sigma_y & 0 \end{pmatrix}, \\ \gamma_3 &= -i \begin{pmatrix} 0 & \sigma_z \\ -\sigma_z & 0 \end{pmatrix}, \quad \gamma_5 = \begin{pmatrix} 1 & 0 \\ 0 & -1 \end{pmatrix} = \gamma_1\gamma_2\gamma_3\gamma_0. \end{aligned} \tag{C.2}$$

The continuum fermion propagator is

$$S(x,y) = \int \frac{d^4p}{(2\pi)^4} \frac{1}{i\not{p} + m} e^{ip\cdot(x-y)}. \tag{C.3}$$

The two Dirac positive-energy, zero-momentum eigenstates are

$$u(\vec{p} = \vec{0}, s) = \frac{1}{\sqrt{2}} \begin{pmatrix} \chi_s \\ \chi_s \end{pmatrix}, \quad \overline{u}(\vec{p} = \vec{0}, s) = \frac{1}{\sqrt{2}} \begin{pmatrix} \chi_s^\dagger & \chi_s^\dagger \end{pmatrix}, \tag{C.4}$$

where

$$\chi_0 = \begin{pmatrix} 1 \\ 0 \end{pmatrix}, \quad \chi_1 = \begin{pmatrix} 0 \\ 1 \end{pmatrix}. \tag{C.5}$$